BOUNDARY ELEMENT METHOD IN SPATIAL CHARACTERIZATION OF THE ELECTROCARDIOGRAM

Matti Stenroos

Dissertation for the degree of Doctor of Science in Technology to be presented with due permission of the Faculty of Information and Natural Sciences, Helsinki University of Technology, for public examination and debate in Auditorium E at Helsinki University of Technology (Espoo, Finland) on the 25th of October, 2008, at 12 o'clock noon.

Abstract

The electrochemical activity of the heart gives rise to an electric field. In electrocardiography, cardiac electrical activity is assessed by analyzing the potential distribution of this field on the body surface. The potential distribution, or the set of measured surface-voltage signals, is called the electrocardiogram (ECG). Spatial properties of the ECG can be captured with body surface potential mapping (BSPM), in which the electrocardiogram is measured using dozens of electrodes. In this Thesis, methods for solving the forward and inverse problems of electrocardiography are developed and applied to characterization of acute myocardial ischemia.

The methodology is based on numerical computation of quasi-static electric fields in a volume conductor model. An open-source Matlab toolbox for solving volume conductor problems with the boundary element method (BEM) is presented. The Galerkin BEM and analytical operator-integrals are, for the first time, applied to the epicardial potential problem; the formulation for a piece-wise homogeneous volume conductor is presented in detail, enabling straightforward inclusion of the lungs or other inhomogeneities in the thorax model.

The results show that errors due to discretization and forward-computation are smaller with the linear Galerkin (LG) method than with the conventional methods. These benefits do, however, not reflect to the Tikhonov-regularized inverse solution. If the lungs are omitted, as commonly is done, the choice of the computational method is not significant.

In a set of 22 patients measured with BSPM during coronary angioplasty (PTCA), the application of a BEM thorax model with dipolar equivalent sources enabled accurate discrimination between occluded coronary arteries: the correct classification was obtained in 21 patients using the BSPM and in 20 patients using a 5-electrode set suggested elsewhere. The ischemic regions could also be localized anatomically correctly with simplified epicardial potential imaging, even though patient-specific thorax models were not used. In another set, comprising 79 acute ischemic patients and 84 controls, dipole-markers performed well in detection and quantification of acute ischemia. These results show that the modeling-approach can provide valuable information also without patient-specific models and complicated protocols.

Tiivistelmä

Sydänlihassolujen sähkökemiallinen toiminta synnyttää sähkökentän. Elektrokardiografiassa sydämen sähköistä toimintaa tutkitaan analysoimalla tämän kentän potentiaalijakaumaa kehon pinnalla. Kehon pintapotentiaalijakaumaa tai siitä mitattua signaalijoukkoa kutsutaan elektrokardiogrammiksi (EKG). Elektrokardiogrammin spatiaaliset piirteet saadaan taltioitua EKG-kartoituksessa, jossa elektrokardiogrammia mitataan kymmenien elektrodien avulla. Tässä väitöskirjassa kehitetään kentänlaskentamenetelmiä elektrokardiografian suoran ja käänteisen ongelman ratkaisuun. Menetelmiä sovelletaan akuutin sydänlihasiskemian karakterisointiin.

Työn metodiikka perustuu kvasistaattisten sähkökenttien numeeriseen laskentaan rintakehän johtavuusmallissa reunaelementtimenetelmän (BEM) avulla. BEM-perustyökaluista on koottu avoimen lähdekoodin Matlab-kirjasto. Galerkinin painotusta ja analyyttisesti laskettuja operaattori-integraaleja sovelletaan ensimmäistä kertaa epikardiaalipotentiaalin reunaelementtiratkaisussa. Tarvittavien yhtälöiden johto ja diskretointi paloittain jatkuvassa väliaineessa esitetään perusteellisesti, mikä mahdollistaa keuhkojen suoraviivaisen sisällyttämisen rintakehämalliin.

Lineaarinen Galerkin-menetelmä pienentää suoran ongelman laskennan ja diskretoinnin aiheuttamia virheitä verrattattuna yleisesti käytettyyn kollokaatiomenetelmään. Nämä hyödyt eivät kuitenkaan heijastu Tikhonov-regularisoinnin avulla laskettuihin käänteisen ongelman ratkaisuihin. Jos keuhkot jätetään mallintamatta, kuten alan tutkimuksessa tapana on, laskentamenetelmän valinnalla ei ole merkitystä.

Sepelvaltimon pallolaajennuksen aikana mitattujen EKG-kartoitusten aineistossa tukkeutunut valtimo kyettiin tunnistamaan BEM-rintakehämallin ja dipolimallinnuksen avulla: 22 potilaasta 21 luokiteltiin oikein EKG-kartoituksen ja 20 erään aiemmin kuvaillun viiden elektrodin joukon avulla. Iskeemiset alueet paikannettiin yksinkertaistetun epikardiaalipotentiaalikuvantamisen avulla anatomisesti oikein — ilman potilaskohtaisia rintakehämalleja. 79 iskemiapotilaasta ja 84 terveestä verrokista koostuvassa aineistossa dipolimalli tuotti lupaavia tuloksia sydänlihasiskemian havaitsemisessa ja infarktivaurion koon arvioinnissa. Tulokset osoittavat, että kentänlaskennallinen lähestymistapa tuottaa hyödyllistä tietoa myös ilman potilaskohtaisia malleja ja monimutkaisia menetelmiä.

Contents

Preface

The research reported in this Thesis was carried out in the cardiac research group of the Laboratory of Biomedical Engineering and Department of Biomedical Engineering and Computational Science (BECS) at Helsinki University of Technology.

List of Publications

This Thesis consists of an overview and the following six Publications.

I. M. Stenroos, V. Mäntynen, and J. Nenonen. A Matlab Library for Solving Quasi-Static Volume Conduction Problems Using the Boundary Element Method. *Computer Methods and Programs in Biomedicine*, 88:256–263, 2007. ©2007 Elsevier.

II. M. Stenroos and J. Haueisen. Boundary Element Computations in the Forward and Inverse Problem of Electrocardiography: Comparison of Collocation and Galerkin Weightings. *IEEE Transactions on Biomedical Engineering*, 55:2124–2133, 2008. ©2008 IEEE.

III. M. Stenroos. Transfer Matrix for Epicardial Potential in a Piece-Wise Homogeneous Thorax Model: the Boundary Element Formulation. *Department of Biomedical Engineering and Computational Science Publications*, Report A04, 9 pages, 2008.

IV. M. Stenroos, M. Lindholm, H. Hänninen, I. Tierala, H. Väänänen, and T. Katila. Dipole Modeling in Electrocardiographic Classification of Acute Ischemia. *Computers in Cardiology 2005*, 32:655–658, 2005. ©2005 IEEE.

V. M. Stenroos, M. Lindholm, P. Vesterinen, M. Kylmälä, T. Konttila, J. Dabek, and H. Väänänen. Electrocardiographic Detection and Quantification of Acute Myocardial Ischemia with Dipole Modeling. *Computers in Cardiology 2006*, 33:29–32, 2006.

VI. M. Stenroos, H. Hänninen, M. Lindholm, I. Tierala, and T. Katila. Lead Field Formulation for Epicardial Potential in Electrocardiographic Localization of Acute Myocardial Ischemia. *IFMBE Proceedings*, 11:2265-1–2265-5, 2005. ©2005 EMBEC'05 & IFMBE.

Copyrighted Publications are reproduced with permission.

Summary of Publications

I. **A Matlab Library for Solving Quasi-Static Volume Conduction Problems Using the Boundary Element Method**
Basic principles of the boundary element method (BEM) are reviewed, and BEM discretization of quasi-static electric potential and biomagnetic volume conduction problems is presented. A Matlab library for solving these problems is described, validated, and applied to various problems. The library is the first free, open-source toolbox for solving this kind of problems with the BEM using the Matlab environment. It is currently in use in over 20 foreign research groups.

II. **Boundary Element Computations in the Forward and Inverse Problem of Electrocardiography: Comparison of Collocation and Galerkin Weightings**
Source-modeling and epicardial potential problems are presented with help of single- and double-layer operators and discretized with both collocation and Galerkin BEMs. In the epicardial potential problem, the Galerkin BEM is presented and analytical operator integrals are used for the first time. The linear Galerkin method yields the smallest errors in discretization and forward computation of the epicardial potential. In the inverse solution, the modeling of lungs has clearly larger effect on results than the choice of the BEM technique does.

III. **Transfer Matrix for Epicardial Potential in a Piece-Wise Homogeneous Thorax Model: the Boundary Element Formulation**
The integral equation system relating the epicardial and body surface potentials in a piece-wise homogeneous thorax model is derived. The equations are presented in terms of single- and double-layer operators, and discretization is done with both collocation and Galerkin BEMs. The derivation is more compact and general and the resulting transfer matrix is mathematically more stable than those in earlier studies.

IV. **Dipole Modeling in Electrocardiographic Classification of Acute Ischemia**
A BEM volume conductor model and dipolar equivalent sources are applied to spatial characterization of the electrocardiogram. The dataset consists of body surface potential mappings (BSPM) measured from 22 patients during coronary angioplasty operations, classified according to the occluded coronary artery. Up to 21 of the 22 patients could be classified to the correct category by comparing the dipole directions.

V. Electrocardiographic Detection and Quantification of Acute Myocardial Ischemia with Dipole Modeling
The BEM and dipole models are used in detection and size estimation of acute myocardial ischemia. Dipoles are fitted to electrocardiographic markers derived from the BSPM data of 79 patients and 84 healthy controls. Various parameters are derived from the dipole vectors. Then, receiver-operating-characteristic curves are used for finding the best-discriminating markers between the patients and controls, and markers providing the best correlations with the CK-Mb mass are sought for.

VI. Lead Field Formulation for Epicardial Potential in Electrocardiographic Localization of Acute Myocardial Ischemia
Epicardial potential imaging is applied to localization of the ischemic region from the same dataset that was used in Publication IV. A simple template-based method is presented; the method provides for robust searching of the center of the ischemic region. Localization results are anatomically correct. This study won the first price in the IFMBE Young Investigator Competition of the EMBEC'05 conference.

Author's Contribution

The author of this Thesis ("the author") was the main investigator and principal writer in all included Publications. The theoretical work and computer programming related to the boundary element method was mainly carried out by the author; only the numerical integration rules and tools for analytical validation were implemented by others.

In Publication I, the author designed and implemented the BEM library and examples, while co-authors performed the validation. In Publication II, the author developed and implemented all computational models and test scenarios; results were interpreted together with the co-author, who also contributed to the study design. In Publications IV–VI, co-authors collected, documented and preprocessed the patient data; the author developed and applied the computational models and analyzed the results.

All Publications were written by the author. Co-authors contributed by reviewing the manuscripts.

List of Abbreviations

ATI	Activation time imaging
BEM	Boundary element method
BSPM	Body surface potential mapping
DOF	Degree of freedom
ECD	Equivalent current dipole
EDL	Equivalent double-layer
ECG	Electrocardiogram or electrocardiography
FEM	Finite element method
CC	Constant collocation method
CG	Constant Galerkin method
LC	Linear collocation method
LG	Linear Galerkin method
RE	Relative error
SMD	Single moving dipole
TMP	Transmembrane potential
UDL	Uniform double-layer

1 Introduction

Electrochemical activity of cardiac muscle cells gives rise to electric and magnetic fields [1]. The electric field is reflected on the body surface as a potential distribution. In electrocardiography, cardiac electrical activity is assessed by studying voltage signals measured on the body surface. The set of measured signals, or more generally, the body surface potential distribution, is called the electrocardiogram (ECG).

In clinical use, the most common electrocardiographic application is the 12-lead ECG [2], which is measured with nine electrodes. The 12-lead ECG is visualized as a set of time-voltage tracings, and spatial analysis is carried out by comparing relative amplitudes of the tracings. From the 12-lead ECG, one can characterize the cardiac rhythm and infer the approximate location and propagation direction of the mean cardiac electrical activity.

In body surface potential mapping (BSPM), the ECG is measured with tens of electrodes, yielding a more accurate spatial sampling of the potential distribution on the thorax than that in the 12-lead ECG. The BSPM data are commonly processed as multi-lead ECG, a collection of time-voltage tracings; quantitative analysis is based on features that are extracted from single leads, while the spatial analysis resides typically on qualitative level, such as visual inspection of the spatial distributions of the single-lead features. With this kind of analysis, geometrical properties of potential distributions and the knowledge of electrode positions are not effectively utilized. Overall, the large dimension of the BSPM data poses a challenge for the analysis.

Challenges of the BSPM analysis are tackled with modeling-approaches, in which the relationship between the cardiac electrical activity and the resulting ECG is characterized. In these approaches, the cardiac electrical activity is represented either with help of a mathematical source model or in terms of epicardial potential. Electrical properties of the thorax are modeled applying anatomical imaging, image processing, electromagnetic theory, and numerical mathematics. Computation of the ECG from a known source model or epicardial potential is commonly referred to as the forward problem of electrocardiography. Respectively, estimation of the sources or epicardial potential from measured ECG data is called the inverse problem of electrocardiography.

The anatomical information needed in the model building is obtained with, *e.g.*, magnetic resonance imaging or X-ray computed tomography. Electri-

cal properties of the thorax are typically assumed piece-wise homogeneous, enabling application of the boundary element method (BEM) in the numerical computations. In order to obtain accurate results, the anatomical and computational models need to be constructed individually for each patient; in addition to imaging and computing facilities, lots of manual work from skilled people is thus needed. The modeling approaches are hereby used primarily for research purposes. Overall, the worlds of clinical electrocardiography and modeling are wide apart.

1.1 Aims and Outline

The primary aim of this Thesis is to develop computational methods and computer program libraries for solving the electrocardiographic forward and inverse problems. The method development is focused on boundary element modeling of the epicardial potential problem.

The secondary aim is to bring simple modeling-approaches of electrocardiography a step closer to the clinical world; to show that modeling can yield valuable information also without individual thorax models, exactly localized electrodes, and complicated analysis protocols.

This Thesis consists of an overview and six Publications. In the overview, the principal aim is to wrap the theory presented in Publications I-III into a compact but thorough package, presenting the source-modeling and epicardial potential problems in the same context and notation for the first time. The overview provides also more background for and some discussion on Publications II and III and an introduction on source-modeling methods. In addition, the methodology and results of Publications IV-VI are summarized, extended, and briefly discussed.

The overview is organized as follows:

- **Chapter 2**: The quasi-static approximation of bioelectromagnetic fields is reviewed, and the principle behind the boundary element method (BEM) is introduced. Computation of electric potential in a volume conductor using the BEM is presented in a compact, but thorough manner.

- **Chapter 3**: Forward and inverse problems of electrocardiography are reviewed: Principles and methodology of source-modeling are intro-

duced, linking to the theory presented in Chapter 2. Epicardial potential imaging is reviewed in more detail; computational methods and volume conductor modeling are treated. As part of the review, the Publications II and III in epicardial potential imaging and Publications IV and V in dipole modeling are placed in the proper context.

- **Chapter 4**: Methods treated in this work are applied to spatial charaterization of myocardial ischemia. First, dipole modeling is applied to detection, coarse localization, and quantification of myocardial ischemia. Then, simplified epicardial potential imaging is used in localization of the ischemic region.

- **Chapter 5**: a summary of and outlook on this Thesis and its main results is given.

2 Volume Conductor Modeling

2.1 Quasi-Static Approximation of Bioelectric Fields

2.1.1 Wave Equations for Potentials

Electromagnetic phenomena are characterized with the Maxwell equations [3]. An electrically active nerve or muscle cell acts as a source of electromotive force that gives rise to electric field and current in the extracellular domain. In macroscopic scale, the sources of these fields can be modeled in terms of primary charge density ρ_p and current density $\vec{J}_\mathrm{p}$ [1]. Biological medium is non-magnetic, conductive, and, at bioelectrical field strengths, electrically linear. With these source and material properties and harmonic time dependency of angular frequency ω, the Maxwell equations are

$$\nabla \cdot \vec{E} = \frac{\rho_\mathrm{p}}{\epsilon} \tag{1}$$

$$\nabla \cdot \vec{B} = 0 \tag{2}$$

$$\nabla \times \vec{E} = i\omega\vec{B} \tag{3}$$

$$\nabla \times \vec{B} = \mu_0\vec{J}_\mathrm{p} + \mu_0(\sigma - i\omega\epsilon)\vec{E}, \tag{4}$$

where $\vec{E}$ is the electric field, $\vec{B}$ is the magnetic induction field, ϵ and σ are the permittivity and conductivity of the medium, μ_0 is the magnetic permeability of vacuum, and i is the complex unit: $i = \sqrt{-1}$. The relationship between the primary charges and currents in homogeneous medium is obtained by taking divergence of Eq. 4 and applying Eq. 1, yielding

$$\frac{\rho_\mathrm{p}}{\epsilon} = \frac{\nabla \cdot \vec{J}_\mathrm{p}}{i\omega\epsilon - \sigma}. \tag{5}$$

In electrocardiography, we are interested in voltages—potential-differences. Hereby it is logical to characterize the cardiac electromagnetic field with potential-functions. From Eqs. 2 and 3, we get expressions for fields in terms of vector potential $\vec{A}$ and scalar potential ϕ:

$$\vec{B} = \nabla \times \vec{A} \tag{6}$$

$$\vec{E} = i\omega\vec{A} - \nabla\phi. \tag{7}$$

Using these relations in Eqs. 1 and 2 and applying the Lorenz gauge [3] gives wave equations for potentials. The general solutions of these equations are

obtained by integrating the source density weighted with the Green function of the wave equation, leading to [4]

$$\vec{A} = \frac{\mu_0}{4\pi} \int_{V_p} \frac{\vec{J_p} e^{ik|\vec{r}-\vec{r}\,'|}}{|\vec{r}-\vec{r}\,'|} \, dV' \tag{8}$$

$$\phi = \frac{1}{4\pi(i\omega\epsilon - \sigma)} \int_{V_p} \frac{(\nabla' \cdot \vec{J_p}) e^{ik|\vec{r}-\vec{r}\,'|}}{|\vec{r}-\vec{r}\,'|} \, dV', \tag{9}$$

where

$$k^2 = \omega^2 \mu_0 \epsilon \left(1 + \frac{i\sigma}{\omega\epsilon} \right), \tag{10}$$

$\vec{r}$ and $\vec{r}\,'$ are position vectors in field and source spaces, respectively, and V_p is the volume containing all primary sources.

In Eq. 4, there are three types of currents: the primary currents $\vec{J_p}$, resistive volume currents $\sigma\vec{E}$, and displacement currents $i\omega\epsilon\vec{E}$. The relative strength of displacement[1] and resistive currents is characterized by the ratio $\omega\epsilon/\sigma$. This ratio defines, whether the medium acts primarily as a conductor or as an insulator, and, whether the wave motion is decaying or propagating. The strength of the inductive coupling in Eq. 3 is also governed by σ, ϵ, and ω.

2.1.2 Electrical Properties of Biological Tissues

Electrical properties of biological tissue depend on frequency and tissue type. In some tissues, *e.g.* muscles, these parameters are also anisotropic due to the directed fibrous structures. Tissue conductivity at frequencies below 1 kHz has been studied, *e.g.*, in [5–8]. Capacitive properties at low frequencies have, to the author's knowledge, been studied only by Schwan and Kay [9,10] and Gabriel *et al.* [8]. Values for permittivity ϵ, conductivity σ, and the amplitude ratio of displacement and resistive currents in various tissue types at three frequencies are given in Table 1. The conductivities reported by Gabriel *et al.* were, in general, lower than those reported by Schwan and Kay.

Measurement of permittivity at low frequencies is prone to errors. The main source of error is polarization that takes place at the electrode–tissue interface [8, 9]. In Table 1, the values marked with asterisk are upper-limit values: in [10] it is written that "The values at 10 cps are possibly 3 to 10 times smaller than quoted". According to Gabriel *et al.* [8], electrode polarization

---

[1]Effects of the displacement currents on the bioelectromagnetic fields are commonly referred to as "capacitive effects".

Table 1: *Electrical properties of biological tissues [8, 10]. The values marked with asterisk are upper-limit estimates.*

10 Hz	Schwan and Kay			Gabriel *et al.*		
	$\epsilon/10^6\epsilon_0$	σ (S/m)	$|\omega\epsilon/\sigma|$	$\epsilon_r/10^6$	σ (S/m)	$|\omega\epsilon/\sigma|$
Heart	20*	0.10	0.100*	23	0.06	0.233
Liver	50*	0.12	0.200*	20	0.03	0.371
Lung	25*	0.09	0.150*	30	0.03	0.596
Muscle	30*	0.10	0.150*	60	0.23	0.148
100 Hz						
Heart	0.82	0.09	0.040	4.00	0.09	0.247
Liver	0.85	0.13	0.035	0.90	0.04	0.125
Lung	0.45	0.09	0.025	1.50	0.05	0.167
Muscle	0.80	0.11	0.035	18.50	0.34	0.303
1000 Hz						
Heart	0.32	0.12	0.150	0.30	0.11	0.152
Liver	0.15	0.13	0.060	0.08	0.04	0.111
Lung	0.09	0.10	0.050	0.10	0.05	0.111
Muscle	0.13	0.12	0.060	0.65	0.45	0.080

may affect their results below 100 Hz by a factor of two or three. These measurements and results are discussed in more detail in [11].

2.1.3 Quasi-Static Approximation

The wave motion is characterized by the exponential term in Eqs. 8 and 9. Applying the Taylor expansion,

$$e^{ik|\vec{r}-\vec{r}'|} = 1 + ik|\vec{r}-\vec{r}'| - \frac{(k|\vec{r}-\vec{r}'|)^2}{2!} + ... \qquad (11)$$

Studying the magnitude of k with values from Table 1, we see that

$$
\begin{aligned}
|k||\vec{r}-\vec{r}'| &= \left|\omega\sqrt{\mu_0\epsilon}\sqrt{1+\frac{i\sigma}{\omega\epsilon}}\right||\vec{r}-\vec{r}'| \qquad (12)\\
&< 0.002, \quad f = 10\,\text{Hz}\\
&< 0.001, \quad f = 100\,\text{Hz}\\
&< 0.017, \quad f = 1000\,\text{Hz}.
\end{aligned}
$$

7

Hence we can approximate that, at frequencies below 100 Hz, $e^{ik|\vec{r}-\vec{r}\,'|} = 1$. This means that a change in the source distribution is assumed to reflect instantaneously into all field points. At higher frequencies, this assumption introduces small errors.

The electric field is calculated from potentials according to Eq. 7, where $i\omega\vec{A}$ corresponds to the inductive component of the field. The relative strength of inductive effects can be studied by calculating the ratio of $\omega\vec{A}$ and $\nabla\phi$ for a differential source element [4, 11]. Such a calculation leads to

$$\frac{|\omega A|}{|\nabla\phi|} \approx (|k||\vec{r}-\vec{r}\,'|)^2. \tag{13}$$

The inductive effects can thus safely be omitted. The electric field can then be calculated from the scalar potential: $\vec{E} = -\nabla\phi$.

According to the ratios presented in Table 1, resistive currents dominate over the displacement currents: Gabriel *et al.* reported [8] that $\omega\epsilon/\sigma$ is at electrocardiographic frequencies larger than 0.1. Both Schwan and Kay [10] and Gabriel *et al.* reported ratios of over 0.15 at 10 Hz, but these results are unreliable. On basis of these results, it is not clear, whether biological tissues can be assumed purely resistive at bioelectric frequencies. As far as the author of this Thesis knows, the error introduced by omitting the displacement currents has not been studied in detail. In [12], the validity of this approximation was studied using a multi-layer spherical model. In that study, however, only small ($\omega\epsilon/\sigma <= 0.004$) or large ($\omega\epsilon/\sigma \approx 1$) ratios were tested. With the smaller ratio, there were no noticeable capacitive effects; with the larger ratio, the effects were clear. Henceworth, this study is based on the conventional assumption that capacitive effects are so small that they can be left out of the calculations without introducing major errors.

When propagative, inductive, and capacitive effects are omitted, the Maxwell equations are simplified to the static form. Because the sources are still time-dependent and conductivity may possess frequency dependency, the concept "quasi-static" is used. The conductivity is commonly assumed independent of the frequency, following the results of [6]. In practice, this means that tissues are not supposed to act as temporal filters. To the author's knowledge, the error introduced by this assumption on common electrocardiographic applications has not been studied; in [12], it was concluded that the frequency dependency of the conductivity may act as a temporal filter on the electroencephalogram and that capacitive effects due to vernix caseosa affect the fetal electrocardiogram.

In summary, the quasi-static Maxwell equations for conductive, non-magnetic, electrically linear material are

$$\nabla \cdot \vec{E} = \frac{\rho_{\mathrm{p}}}{\epsilon} \tag{14}$$

$$\nabla \cdot \vec{B} = 0 \tag{15}$$

$$\nabla \times \vec{E} = 0 \tag{16}$$

$$\nabla \times \vec{B} = \mu_0(\vec{J}_{\mathrm{p}} + \sigma \vec{E}). \tag{17}$$

Taking divergence of Eq. 17 and applying $\vec{E} = -\nabla\phi$ yields the Poisson equation in terms of primary-current sources:

$$\nabla \cdot (\sigma \nabla \phi) = \nabla \cdot \vec{J}_{\mathrm{p}}. \tag{18}$$

2.2   Boundary Element Method

The boundary element method is mathematically based on the method of weighted residuals [13]: Consider the problem

$$L[f](\vec{r}) = g(\vec{r}), \tag{19}$$

where L is a differential or integral operator, g is a known function, and f is the unknown function that L acts on. First, approximate f as a linear combination of N basis functions $\psi_j(\vec{r})$ and insert the approximation to the original equation:

$$f(\vec{r}) \approx \sum_{j=1}^{N} \varphi_j \psi_j(\vec{r}) \tag{20}$$

$$\Rightarrow \sum_{j=1}^{N} \varphi_j L[\psi_j](\vec{r}) - g(\vec{r}) = R_N(\vec{r}), \tag{21}$$

where R_N is the residual of the approximated solution. Then, force the residual to zero with respect to N weight functions $w_i(\vec{r})$ over the solution domain Ω:

$$\int_{\Omega} R_N(\vec{r}) w_i(\vec{r}) d\Omega = 0 \tag{22}$$

$$\Rightarrow \sum_{j=1}^{N} \varphi_j \int_{\Omega} w_i(\vec{r}) L[\psi_j](\vec{r}) d\Omega = \int_{\Omega} w_i(\vec{r}) g(\vec{r}) d\Omega. \tag{23}$$

Now the discretized problem can be written in matrix form:

$$\mathbf{L}\boldsymbol{\Phi} = \mathbf{g}, \tag{24}$$

where $\boldsymbol{\Phi}$ and $\mathbf{g}$ are $N \times 1$–vector with elements φ_i and $g_i = \int_\Omega w_i(\vec{r})g(\vec{r})d\Omega$, respectively, and $\mathbf{L}$ is an $N \times N$ matrix with elements

$$L_{ij} = \int_\Omega w_i(\vec{r})L[\psi_j](\vec{r})d\Omega. \tag{25}$$

The coefficients φ_j are, in principle, solved from Eq. 24 by inverting the matrix $\mathbf{L}$.

The most simple choice for the weight function is the Dirac δ function. With this choice, the error is minimized in a discrete set of points [13]. This approach is called the point collocation method, and the definition points of the δ functions are referred to as the collocation points. The collocation method provides for a computationally efficient solution of the residual-minimization problem: the integrals in previous equations are simplified to evaluations of the integrands at the definition points of the δ functions. The residual can also be minimized over the whole domains instead of discrete points. This is the aim of the Galerkin method, in which the weight functions are chosen identical to the basis functions [13]. The points, around which the Galerkin solution is spanned are the same as the collocation points. The Galerkin solution is, however, not optimized for accuracy in these points.

In the boundary element methods used in this work, the governing partial differential equations are first converted to surface integral form. Then, the basis and weight functions are defined on triangulated boundary surfaces, leading to a linear equation array that yields potentials on the boundary surfaces. The boundary element method is discussed in more detail in [13] and in Publications I and II.

The boundary element method was for the first time applied to electrocardiographic potential problem in [14, 15]. The terminology and notation used in those studies was different from those used in this Thesis, but effectively, constant basis functions with Galerkin weighting were used.

2.3 Surface Integral Equations for Electric Potential

In this Section, a compact, but thorough presentation on integral equations and discretization of the epicardial potential and source-modeling problems

is given. More background and discussion can be found in Section 3 and in Publications I–III.

In this presentation, geometry and electrical parameters are kept apart with help of operator notation. The use of single- and double-layer operators facilitates understanding of the equations and, especially, implementation of the boundary-element discretization. Moreover, with effective use of the operators, both collocation and Galerkin problems can be presented with the same set of equations.

The Galerkin discretization of the epicardial potential problem was for the first time presented in Publications II and III. In addition, the Galerkin discretization of the source-modeling problem is, to the author's knowledge, in this Thesis presented for the first time in pure matrix-vector form.

2.3.1   Principle and Notation

The quasi-static potential problem in a piece-wise homogeneous volume conductor obeys the Poisson equation

$$\nabla(\sigma\nabla\phi) = \nabla \cdot \vec{J}_{\mathrm{p}} \tag{26}$$

with two boundary conditions: the potential ϕ and normal component of the current density $-\sigma\nabla\phi$ are continuous. The geometry of the problem is illustrated in Fig. 1. Proceeding towards the boundary element method, the Poisson equation is converted to surface integral form with help of the Green theorem. First, apply the free-space Green function $\frac{1}{4\pi|\vec{r}-\vec{r}\,'|}$ and the electric potential ϕ to the Green theorem:

$$\int\limits_{V} \frac{1}{|\vec{r}-\vec{r}\,'|}\nabla\,'^2\phi(\vec{r}\,') - \phi(\vec{r}\,')\nabla\,'^2\frac{1}{|\vec{r}-\vec{r}\,'|}\,dV' =$$

$$\oint\limits_{\partial V} \left[\frac{1}{|\vec{r}-\vec{r}\,'|}\nabla\,'\phi(\vec{r}\,') - \phi(\vec{r}\,')\frac{(\vec{r}-\vec{r}\,')}{|\vec{r}-\vec{r}\,'|^3}\right] \cdot d\vec{S}\,', \tag{27}$$

where V is the volume of integration, ∂V is the boundary of V, and $d\vec{S}$ is the differential surface element multiplied with the exterior surface normal: $d\vec{S} = \vec{n}\,dS$. Then, restrict V to an electrically homogeneous compartment V^l of the volume conductor, apply the Poisson equation, and simplify to get

$$K^l(\vec{r})\phi(\vec{r}) \;\; = \;\; \frac{1}{4\pi}\int\limits_{V^l} \frac{\vec{J}_{\mathrm{p}} \cdot (\vec{r}-\vec{r}\,')}{|\vec{r}-\vec{r}\,'|}\,dV' +$$
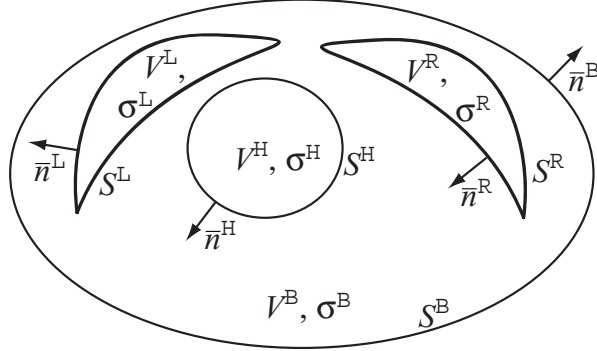
Figure 1: *The piece-wise homogeneous model of the thoracic volume conductor; S^l labels the exterior boundary surface of the volume V^l, and σ^k is the conductivity in V^k. Superscripts mark the surfaces as follows: H is the epicardial (heart), L is the left lung, R is the the right lung, and B is the body surface. Normal vector $\vec{n}^l$ points outwards from volume V^l.*

$$\frac{1}{4\pi} \oint_{\partial V^l} \left[\frac{1}{|\vec{r} - \vec{r}\,'|} \nabla'\phi(\vec{r}\,') - \phi(\vec{r}\,') \frac{(\vec{r} - \vec{r}\,')}{|\vec{r} - \vec{r}\,'|^3} \right] \cdot d\vec{S}\,', \quad (28)$$

where, with help of the Dirac δ function and limiting-value analysis [16, 17],

$$K^l(\vec{r}) = \begin{cases} 1, & \vec{r} \in V^l \\ 1/2, & \vec{r} \in \partial V^l \\ 0, & \vec{r} \notin \overline{V^l}. \end{cases} \quad (29)$$

Surface integral equations for potential are derived by first applying Eq. 28 in each compartment of interest with the field point $\vec{r}$ on each boundary surface S^l and then eliminating uninteresting variables with help of the boundary conditions. This process is more thoroughly described in [1, 14, 18] and in Publication III.

The integral equations are in this study presented with help of single- and double-layer operators G and D:

$$G^{kl}[f](\vec{r}) = \frac{1}{4\pi} \int_{S^l} \frac{f(\vec{r}\,')}{|\vec{r} - \vec{r}\,'|} dS', \quad \vec{r} \in S^k \quad (30)$$

$$D^{kl}[g](\vec{r}) = \frac{1}{4\pi} \int_{S^l} g(\vec{r}\,') \frac{(\vec{r} - \vec{r}\,')}{|\vec{r} - \vec{r}\,'|^3} \cdot d\vec{S}\,', \, \vec{r} \in S^k, \quad (31)$$

where superscripts k and l label the field and source surfaces, respectively. Surfaces are labeled with S; f and g refer to functions that the operators act

on. In some of the following equations, the field point is in the volume, not on boundary surfaces. In those cases, only the source surface is labeled in the operator relation; for example,

$$D^l[g](\vec{r}) = \frac{1}{4\pi} \int_{S^l} g(\vec{r}') \frac{(\vec{r} - \vec{r}')}{|\vec{r} - \vec{r}'|^3} \cdot d\vec{S}'. \tag{32}$$

In the following, surface integral equations are presented and discretized. The surfaces are labeled by superscripts, whereas subscripts mark elements of vectors or matrices. Discretized variables are presented as column vectors, printed in boldface.

2.3.2 Integral Equation for Electric Potential in Terms of Infinite-Medium Potential

In a piece-wise homogeneous volume conductor with N boundary surfaces and a known primary current distribution inside the conductor, the integral equation for potential on surface k [1, 14, 18] is

$$\phi^k(\vec{r}) = \frac{2\sigma_s}{\sigma_-^k + \sigma_+^k} \phi_\infty^k(\vec{r}) - 2 \sum_{l=1}^{N} \frac{\sigma_-^l - \sigma_+^l}{\sigma_-^k + \sigma_+^k} D^{kl}[\phi^l], \tag{33}$$

and the corresponding equation for a field point not on a conductivity boundary is [1, 19]

$$\sigma(\vec{r})\phi(\vec{r}) = \sigma_s \phi_\infty(\vec{r}) - \sum_{l=1}^{N} (\sigma_-^l - \sigma_+^l) D^l[\phi^l](\vec{r}), \tag{34}$$

where σ_-^i and σ_+^i are conductivities inside and outside surface i, and ϕ_∞^i is the potential generated on surface i by sources in infinite, homogeneous medium of conductivity σ_s. When these sources are modeled with primary currents $\vec{J}_\mathrm{p}$, the infinite-medium potential ϕ_∞ is

$$\phi_\infty(\vec{r}) = \frac{1}{4\pi\sigma_s} \int_{V_s} \frac{\vec{J}_\mathrm{p} \cdot (\vec{r} - \vec{r}')}{|\vec{r} - \vec{r}'|^3} \, dV', \tag{35}$$

where V_s is the volume containing all primary sources.

Application of basis functions ψ and weight functions w to Eq. 33 leads to

$$\mathbf{A}^k \mathbf{\Phi}^k = b^k \mathbf{B}^k - \sum_{l=1}^{N} c^{kl} \mathbf{D}^{kl} \mathbf{\Phi}^l, \tag{36}$$

13

in which

$$b^k = \frac{2\sigma_s}{\sigma_-^k + \sigma_+^k}, \quad c^{kl} = 2\frac{\sigma_-^l - \sigma_+^l}{\sigma_-^k + \sigma_+^k}, \tag{37}$$

and the matrices $\mathbf{A}^k$ and $\mathbf{D}^{kl}$ and vector $\mathbf{B}^k$ are as described in Table 2 [2]. With flat triangular elements and polynomial basis functions, all operator integrals can be calculated analytically [20–23]. Writing discretized integral equations for all boundary surfaces and collecting them into matrix form yields

$$
\overbrace{\begin{pmatrix} \mathbf{A}^1 & & & \\ & \mathbf{A}^2 & & \\ & & \ddots & \\ & & & \mathbf{A}^N \end{pmatrix}}^{\mathbf{A}} \begin{pmatrix} \mathbf{\Phi}^1 \\ \mathbf{\Phi}^2 \\ \vdots \\ \mathbf{\Phi}^N \end{pmatrix} =
$$

$$
\overbrace{\begin{pmatrix} b^1\mathbf{B}^1 \\ b^2\mathbf{B}^2 \\ \vdots \\ b^N\mathbf{B}^N \end{pmatrix}}^{\mathbf{B}} - \overbrace{\begin{pmatrix} c^{11}\mathbf{D}^{11} & c^{12}\mathbf{D}^{12} & \cdots & c^{1N}\mathbf{D}^{1N} \\ c^{21}\mathbf{D}^{21} & \ddots & & \vdots \\ \vdots & & \ddots & \vdots \\ c^{N1}\mathbf{D}^{N1} & \cdots & \cdots & c^{NN}\mathbf{D}^{NN} \end{pmatrix}}^{\mathbf{D}} \begin{pmatrix} \mathbf{\Phi}^1 \\ \mathbf{\Phi}^2 \\ \vdots \\ \mathbf{\Phi}^N \end{pmatrix}. \tag{38}
$$

Factoring the terms gives

$$(\mathbf{A} + \mathbf{D})\mathbf{\Phi} = \mathbf{B}, \tag{39}$$

from which $\mathbf{\Phi}$ is solved by inverting the left-side matrix. In case of a finite volume conductor, the matrix $(\mathbf{A} + \mathbf{D})$ is, however, singular due to the unspecified zero level of the potential. The zero potential is set with aid of deflation [24, 25], after which the matrix can be inverted with standard techniques. The discretization process is treated in more detail in Publication I, and methods for calculating the element integrals are discussed in Publications I and II. Methods for solving this problem and the corresponding biomagnetic problem with the collocation BEM are collected to an open-source Matlab toolbox "Helsinki BEM library", presented in Publication I.

---

[2]$\mathbf{A}^k$ can actually be interpreted as a discretized unitary operator

14

Table 2: *Elements of the matrices resulting from discretization with constant collocation (CC), constant Galerkin (CG), linear collocation (LC), and linear Galerkin (LG) methods. $\Omega_j^l(\vec{r})$ is the solid angle spanned by triangle j of surface l at $\vec{r}$, and $\vec{v}_i^k$ is the ith vertex of surface k. T_i^k labels triangle i of surface k, A_i^k the area and $\vec{c}_i^k$ the centroid of that triangle.*

	$\mathbf{D}_{ij}^{kl}$	$\mathbf{G}_{ij}^{kl}$	$\mathbf{A}_{ij}^{k}$	$\mathbf{B}_i^k$
General	$\int\limits_{S^k} w_i^k D^{kl}[\psi_j^l]\, dS$	$\int\limits_{S^k} w_i^k G^{kl}[\psi_j^l]\, dS$	$\int\limits_{S^k} w_i^k \psi_j^k\, dS$	$\int\limits_{S^k} w_i^k \phi_\infty\, dS$
CC	$\Omega_j^l(\vec{c}_i^k)$	$G^{kl}[\psi_j^l](\vec{c}_i^k)$	δ_{ij}	$\phi_\infty(\vec{c}_i^k)$
LC	$D^{kl}[\psi_j^l](\vec{v}_i^k)$	$G^{kl}[\psi_j^l](\vec{v}_i^k)$	δ_{ij}	$\phi_\infty(\vec{v}_i^k)$
CG	$\int\limits_{T_i^k} \Omega_j^l(\vec{r})\, dS$	$\int\limits_{T_i^k} G^{kl}[\psi_j^l]\, dS$	$A_i^k \delta_{ij}$	$\int\limits_{T_i^k} \phi_\infty\, dS$
LG	$\int\limits_{N_i^k} \psi_i D^{kl}[\psi_j^l]\, dS$	$\int\limits_{N_i^k} \psi_i G^{kl}[\psi_j^l]\, dS$	$\int\limits_{N_i^k} \psi_i^k \psi_j^k\, dS$	$\int\limits_{N_i^k} \psi_i^k \phi_\infty\, dS$

2.3.3 Integral Equations for Electric Potential Outside the Source Region

If the sources of the electric field are not in the region of interest and the potential or the normal derivative of the potential is known on any surface circumventing the source distribution, the integral equations for the electric potential outside the source region can be stated without any source model. In electrocardiographic problems, the primary sources are in the heart muscle; the potential outside the heart can then be specified in terms of the epicardial potential. In a homogeneous thoracic volume conductor model, this potential problem is formulated as an equation pair [17, 26]

$$\frac{1}{2}\phi^{\mathrm{H}} = -D^{\mathrm{HB}}[\phi^{\mathrm{B}}] + D^{\mathrm{HH}}[\phi^{\mathrm{H}}] - G^{\mathrm{HH}}[\Gamma^{\mathrm{H}}] \tag{40}$$

$$\frac{1}{2}\phi^{\mathrm{B}} = -D^{\mathrm{BB}}[\phi^{\mathrm{B}}] + D^{\mathrm{BH}}[\phi^{\mathrm{H}}] - G^{\mathrm{BH}}[\Gamma^{\mathrm{H}}], \tag{41}$$

where $\Gamma^{\mathrm{H}} = \partial\phi^{\mathrm{H}}/\partial n$ is the normal component of the potential-gradient on the epicardial surface, and superscripts label surfaces as presented in Fig. 1.

15

The forward transfer matrix for the epicardial potential is commonly formed by discretizing Eqs. 40 and 41, eliminating the $\mathbf{\Gamma}$-term and then solving for $\mathbf{\Phi}$:

$$\mathbf{\Phi}^{\mathrm{B}} = \mathbf{L}\mathbf{\Phi}^{\mathrm{H}}, \tag{42}$$

where

$$\mathbf{L} = \left[\left(\frac{1}{2}\mathbf{A}^{\mathrm{B}} + \mathbf{D}^{\mathrm{BB}}\right) - \mathbf{G}^{\mathrm{BH}}(\mathbf{G}^{\mathrm{HH}})^{-1}\mathbf{D}^{\mathrm{HB}}\right]^{-1} \cdot \tag{43}$$
$$\left[\mathbf{D}^{\mathrm{BH}} + \mathbf{G}^{\mathrm{BH}}(\mathbf{G}^{\mathrm{HH}})^{-1}\left(\frac{1}{2}\mathbf{A}^{\mathrm{H}} - \mathbf{D}^{\mathrm{HH}}\right)\right].$$

Matrix elements are, again, described in Table 2.

When the lower conductivity of the lungs is taken into account, the problem is stated as a system of four integral equations. This system is derived and discretized in Publication III. After discretization and factorization, we get

$$\mathbf{g} = \mathbf{L}\mathbf{\Phi}^{\mathrm{H}}, \tag{44}$$

in which

$$\mathbf{L} = \mathbf{S}^{-1}\mathbf{T}, \tag{45}$$

$$\mathbf{S} = \begin{pmatrix} \mathbf{G}^{\mathrm{HH}} & c_-^{\mathrm{L}}\mathbf{D}^{\mathrm{HL}} & c_-^{\mathrm{R}}\mathbf{D}^{\mathrm{HR}} & \mathbf{D}^{\mathrm{HB}} \\ \mathbf{G}^{\mathrm{LH}} & \frac{c_+^{\mathrm{L}}}{2}\mathbf{A}^{\mathrm{L}} + c_-^{\mathrm{L}}\mathbf{D}^{\mathrm{LL}} & c_-^{\mathrm{R}}\mathbf{D}^{\mathrm{LR}} & \mathbf{D}^{\mathrm{LB}} \\ \mathbf{G}^{\mathrm{RH}} & c_-^{\mathrm{L}}\mathbf{D}^{\mathrm{RL}} & \frac{c_+^{\mathrm{R}}}{2}\mathbf{A}^{\mathrm{R}} + c_-^{\mathrm{R}}\mathbf{D}^{\mathrm{RR}} & \mathbf{D}^{\mathrm{RB}} \\ \mathbf{G}^{\mathrm{BH}} & c_-^{\mathrm{L}}\mathbf{D}^{\mathrm{BL}} & c_-^{\mathrm{R}}\mathbf{D}^{\mathrm{BR}} & \mathbf{D}^{\mathrm{BB}} + \frac{1}{2}\mathbf{A}^{\mathrm{B}} \end{pmatrix}$$

$$\mathbf{g} = \begin{pmatrix} \mathbf{\Gamma}^{\mathrm{H}} \\ \mathbf{\Phi}^{\mathrm{L}} \\ \mathbf{\Phi}^{\mathrm{R}} \\ \mathbf{\Phi}^{\mathrm{B}} \end{pmatrix}, \quad \mathbf{T} = \begin{pmatrix} \mathbf{D}^{\mathrm{HH}} - \frac{1}{2}\mathbf{A}^{\mathrm{H}} \\ \mathbf{D}^{\mathrm{LH}} \\ \mathbf{D}^{\mathrm{RH}} \\ \mathbf{D}^{\mathrm{BH}} \end{pmatrix} \tag{46}$$

with

$$c_+^k = \frac{\sigma^k}{\sigma^{\mathrm{B}}} + 1 \tag{47}$$

$$c_-^k = \frac{\sigma^k}{\sigma^{\mathrm{B}}} - 1. \tag{48}$$

From Eq. 44, the transfer matrix between the epicardial and body surface potentials is obtained by taking the N^{B} last rows of the matrix $\mathbf{L}$.

3 Forward and Inverse Problems of Electrocardiography

3.1 Source Modeling

In this Section, the most common source-modeling approaches used in electrocardiography are reviewed. The weight is on studies that either connect closely with this study or have been applied to characterization of measured ECG datasets. Thus, *e.g.*, computer heart models are not treated.

3.1.1 Principle

Treatment of a bioelectrical source-modeling problem is started by choosing a suitable representation for the primary current distribution $\vec{J}_{\mathrm{p}}$. These source models aim at modeling essential properties of the underlying electrical activity while providing a feasible framework for computations. The optimal source model depends on the specific application: for example, the earliest ventricular activation of a focal arrhythmia may be localized with a point-like source model, but accurate simulation of an ischemic electrocardiogram demands modeling of events on the cellular membrane at ion-current level.

In the boundary element formulation, the general form of a source model is presented in Eq. 35, in which the infinite-medium potential is reconstructed by integrating the primary current density over the source volume, weighted with the appropriate Green function. Practical applications are restricted, simplified, and optimized forms of this equation. In general, the primary current density is first discretized either to a set of point-like elementary current sources or to a linear combination of N_{s} basis functions:

$$\vec{J}_{\mathrm{p}}(\vec{r}\,') = \sum_{j=1}^{N_{\mathrm{s}}} J_{\mathrm{p},j}\vec{\psi}_j(\vec{r}\,'), \tag{49}$$

where $\vec{\psi}_j(\vec{r}\,')$ is a normalized vector-form basis function and $J_{\mathrm{p},j}$ is the amplitude of the jth term of the discretized primary current distribution. The surface potential can then be written as a linear combination of N_{s} transfer coefficients L_i

$$\phi(\vec{r}) = \sum_{j=1}^{N_{\mathrm{s}}} J_{\mathrm{p},j}L_j(\vec{r}), \tag{50}$$

where $L_j(\vec{r})$ is the surface potential generated by the basis function $\vec{\psi}_j$. For a set of N_f surface points, the potential $\mathbf{\Phi}$ can be written with help of a so-called lead-field matrix (LFM) $\mathbf{L}$

$$\mathbf{\Phi} = \mathbf{L}\mathbf{J}_p, \tag{51}$$

where $\mathbf{J}_p$ contains the components $J_{p,j}$ of the modeled source and $\mathbf{L}_{ij} = L_j(\vec{r}_i)$. With this lead-field matrix, it is straightforward and computationally efficient to calculate the surface potential due to any modeled source (the forward problem).

Reconstruction of the modeled source from the known surface potential (the inverse problem) is done by inverting the mapping of Eq. 51. While the solution of the forward problem is unique and, in principle, easy to compute, the inverse problem is ill-posed [27] and it does not have a unique solution [28]. In order to obtain a feasible source-reconstruction, one needs to restrict the solution space and often guide the solution to the preferred direction; these tasks are partially carried out when choosing the source model. If the degree-of-freedom (DOF) of the source model is smaller than the DOF of the data, the source reconstruction can be performed in least-squares sense:

$$\mathbf{J}_p = \mathbf{L}^{\dagger}\mathbf{\Phi}, \quad \text{where} \quad \mathbf{L}^{\dagger} = (\mathbf{L}^T\mathbf{L})^{-1}\mathbf{L}^T. \tag{52}$$

When the DOF of the source model is small, it may be necessary to search for the optimal discretization points of the source model. The relationship between the positions of elementary sources and their contribution to the forward solution is non-linear. When source-positions are optimized, the problem is typically solved in two steps: the position-search is carried out with a non-linear optimization method, and for each test-position, the source amplitudes are computed with linear fitting as described above.

With distributed source models, the DOF of the source is typically larger than the DOF of the data, leading to an under-determined problem. In such a case, the source estimation is commonly done by means of minimum-norm estimate [29] combined with some regularization method. In this Thesis, the truncated singular value decomposition (tSVD) and Tikhonov regularizations are used; principles of these and other regularization methods are presented in [27].

3.1.2 Dipole and Multipole Models

The equivalent current dipole (ECD) is the most simple source model: the whole primary current distribution is characterized with one current dipole $\vec{Q}$,

$$\vec{J}_{\mathrm{p}} = \vec{Q}\delta(\vec{r}\,'), \tag{53}$$

leading to the infinite-medium potential

$$\phi_{\infty} = \frac{1}{4\pi\sigma}\frac{\vec{Q}(\vec{r}\,') \cdot (\vec{r} - \vec{r}\,')}{|\vec{r} - \vec{r}\,'|^3}, \tag{54}$$

in which $\vec{r}\,'$ is the position of the dipole. The dipole position may be either fixed or time-varying (single moving dipole, SMD). With a moving dipole, the problem has three linear and three non-linear components.

In 1913, Einthoven *et al.* [30] characterized the mean direction of the cardiac electric activation with a two-dimensional vector that can be reconstructed with help of the triangle hypothesis from measurements performed with three electrodes. Quantitative framework for this "heart vector" and its relation to some ECG leads was developed in [31–33]: phantom experiments with a physical dipole source were performed, and the forward and inverse relationships between the three-dimensional dipolar source and four electrocardiographic leads were formulated. These results can be interpreted as the first elecrocardiographic forward and inverse solutions, performed in terms of a pre-fixed ECD. Later, the single moving dipole (SMD) model became more popular, yielding also an estimate for the location of cardiac electrical events.

The inadequacy of the dipole as a model of the cardiac electrical generator was realized in 1948 [33]. Non-dipolar features of the human ECG were later demonstrated in [34]. The clinical interpretation of the spatial properties of the ECG is, however, still strongly based on the concept of heart vector. The Frank leadset [35] is the most widely-spread application for quantitative characterization of the heart vector; the mutually orthogonal Frank leads X, Y, and Z are reconstructed from measurements performed with seven electrodes. The transfer coefficients for these leads were defined according to phantom studies with a physical dipole source [35].

Applications of SMD [36–45] can be divided into two partially overlapping categories: source localization and so-called dipole ranging. In source localization, limitations of the dipole source are recognized, and the method is applied with somewhat focal sources, *e.g.*, small infarctions [36], ectopic

foci [38] or accessory pathways [40]. The SMD has also been used for localizing a pacing catheter [42], and the suitability of the SMD model for guiding a catheter towards the arrhythmia focus is being studied [43–45]. In dipole ranging, a dipole is fitted to the ECG at each time-instant, and dipole parameters (moment, position) are analyzed as time–amplitude plots as in conventional ECG analysis [37, 39]. The best results with the dipole ranging method have been obtained with focal data [36, 37].

In many early SMD studies, *e.g.*, [36, 37, 39], the volume conductor modeling has been performed in homogeneous thorax models using the Gabor–Nelson equations [46]. With these equations, the equivalent dipole inside a homogeneous volume conductor can be defined via integration of the surface potential; inhomogeneities can not be modeled, and the potential has to be known or interpolated over the whole surface. In [41], dipole localization was studied using a BEM model and a two-step dipole fitting procedure (position search with non-linear optimization, moment fitted with linear least squares method); this method was found preferable to the Gabor–Nelson approach. Studies [38, 42] were carried out using the BEM.

In Publications IV and V, dipole models were used in detection, classification, and size-quantification of myocardial ischemia from multi-channel ECG data using the BEM (see Section 4.3). The dipole hypothesis in these studies rose from dipolar patterns in body surface potential distributions; the aim was neither to model or localize the physiological source of the cardiac electrical activity nor to study the behavior of the heart vector in time domain. Instead, the dipole was used as a tool for characterizing the spatial properties of the body surface potential distribution, for performing a physics-based geometrical dimension-reduction on the multi-electrode data. The application of the dipole in these Publications is thus more related to Einthoven's [30] or Frank's [35] concept of the heart-vector than to the other dipole studies reviewed in the previous paragraphs.

The next step in the model complexity is the multipole model, in which the infinite-medium or boundary potential is written as a multipole series that contains at least the dipole and quadrupole terms. The multipole approach of source-modeling has not been used recently, perhaps due to the lack of physiological or geometrical meaning in case of the higher-order multipole components. The use of a high-order multipole model can thus be interpreted rather as dimension-reduction than as a source model. In magnetocardiography, the second-order multipole model (dipole and quadrupole) has performed better than the dipole model in localization of a pre-excitation

site [47]. The use of dipole and multipole models in electrocardiography is reviewed in [48].

3.1.3 Distributed Source Models

In distributed source models, the primary current density is modeled as either a volume or a surface distribution. In volume source models, the primary current density is discretized in the myocardial volume, while in surface source models, the sources may lie on endo- or epicardial, or on both of these surfaces. The directions of the elementary sources can be either free or restricted.

In the review [48], "multiple dipole models" are treated. In some of these models, each dipole represents the mean electrical activity of a specific cardiac region; such an approach can as well be interpreted as discretization of the primary current distribution. Thus, [48] serves also as a review on early studies on distributed source models. A volume source model has later been used for, *e.g.*, estimation of the viable myocardium from electro- and magnetocardiographic data [49]. In one example in Publication I, a surface source model spanned at the endo- and epicardium is used for localization of a region of simulated myocardial ischemia.

The equivalent double-layer model (EDL) [50–53] is an application of the surface source model, in which a simple model of cardiac depolarization is utilized: A depolarization wavefront is modeled as a uniform double-layer (UDL). As long as this layer is closed, it produces no external potential. When the wavefront reaches either the endo- or epicardium, the double-layer opens up, contributing to the electrocardiogram. The open double-layer can be modeled as a sum of a closed layer and an oppositely-directed open UDL at the region of the opening. Thus, the source of the external potential can be modeled as an equivalent double-layer spanned at endo- and epicardial surfaces. The infinite-medium potential due to the EDL can then simply be stated in terms of the double-layer operator,

$$\phi_\infty = \frac{1}{\sigma_s} D^{\mathrm{H}}[s^{\mathrm{H}}], \tag{55}$$

where H is the union of endo- and epicardial surfaces and s^{H} is the EDL strength (the normal component of the primary current). The tools that are used in Section 2.3.2 apply also to discretization of the EDL source.

The bidomain theory of the cardiac muscle [51, 54] provides the theoretical framework for the double-layer source model: In the bidomain theory, the cardiac muscle is modeled as a continuum of intertwined intra- and extracellular spaces that are connected via currents passing through the cell membrane. With help of this theory, the relationship between the primary current $\vec{J}_{\mathrm{p}}$ and the transmembrane potential (TMP) ϕ_m can be written [54]

$$\vec{J}_{\mathrm{p}} = -\sigma_i \nabla \phi_m, \tag{56}$$

where σ_i is the intracellular conductivity. In a homogeneous compartment of cardiac tissue, the infinite-medium potential generated by the volume TMP can be written directly in terms of the surface TMP [51, 52]:

$$\phi_\infty = -\frac{\sigma_i}{\sigma_s} D^{\mathrm{H}}[\phi_m]. \tag{57}$$

The connection between the surface TMP and the extracellular potential enables the use of knowledge on cardiac action potential. This feature is utilized effectively in applications of the EDL. The EDL method has, in addition to depolarization, also been applied to the repolarization [52]. In the ECGSIM program[3] [53], simulation of the electrocardiogram is based on endo- and epicardial action potential waveforms that can be altered in time and shape. The volume conductor modeling in [50, 52, 53] is performed with the boundary element method, applying the point collocation weighting and taking into account the effects of lungs and intracardiac bloodmasses.

In activation time imaging (ATI) and its application "Noninvasive Imaging of Cardiac Electrophysiology" (NICE) [55], the TMP model is utilized in inverse reconstruction of cardiac activation times. In simulation study [25], pre-defined action potential waveform and a time-course model of the ventricular depolarization were coupled with both point collocation and Galerkin BEMs; the Galerkin method performed better in the forward computation due to the more accurate reproduction of the depolarization-time information. This benefit did, however, not reflect to results of [56], in which ATI was performed on a patient with Wolff–Parkinson–White (WPW) syndrome using both collocation and Galerkin BEMs and the FEM; all methods produced very similar activation time maps. The ATI method has been successfully applied to localization of a WPW accessory pathway [55–57] and of a surface breakthrough of paced data in the right atrium [58] and in the right ventricle [56]. Activation time maps obtained from healthy volunteers have been morphologically similar to those obtained earlier from isolated human hearts [57].

---

[3]ECGSIM was used in Publication I for simulating the ischemic electrocardiogram.

3.2 Epicardial Potential Imaging

In epicardial potential imaging [17, 26, 59–61], the electric potential on the surface of the heart outside the myocardium is reconstructed from electro-cardiographic data. Formulating the cardiac inverse problem in terms of epicardial potential instead of using source models has four kinds of advantages [62]:

1. The solution is unique: if the potential is known over any closed surface comprising all sources, potential anywhere outside the source region is uniquely defined.

2. No restrictive assumptions regarding the nature and complexity of sources are made.

3. Intracardiac blood masses and cardiac anisotropy are taken into account implicitly—they do not need to be modeled.

4. Inverse solutions can be validated by comparing them to invasively measured epicardial electrograms.

Although the epicardial potential problem has a unique solution, the problem is ill-posed, and the inverse problem needs to be solved with help of similar regularization methods that are used in source-modeling problems [27].

3.2.1 Computational Methods in Epicardial Potential Imaging

The epicardial potential problem was for the first time formulated for a realistically-shaped geometry in [26] using a collocation BEM approach, in which the potential was approximated with constant basis functions, but the collocation points were placed in the nodes instead of the triangle centroids of the mesh. Other early methods and applications are reviewed in [62], in which simulations with an eccentric-spheres model are presented as well.

Linear collocation BEM has been applied to the epicardial potential problem in, *e.g.*, [17,63] and almost all studies of the Rudy research group [64]. In [17], performances of the constant and linear collocation methods were compared using simulated data; the constant method was found more accurate. These results are discussed in more detail in Publication II, in which the same Dalhousie thorax model as in [17] was used. Second-order basis functions have recently been applied with the collocation method, leading to encouraging

results [64]: With a canine heart and a thorax-shaped saline tank, the reconstruction error of the electrograms over the cardiac cycle decreased by approximately 20 percentage units compared to the linear basis. In a paced human heart, the quadratic method localized the pacing site more accurately than the linear method did. In addition to the BEM, also the finite element method (FEM) [65] and a combined FEM–BEM approach [66] have been suggested. These methods have not gained popularity yet, but they enable the important possibility to model anisotropic structures. Thus far such information is not routinely available, but this may change in the near future due to the development of diffusion-tensor magnetic resonance imaging.

In Publication II, the Galerkin BEM was applied to the epicardial potential problem for the first time. In computation of the single-layer element integrals, analytical formulas [22] were used for the first time, eliminating one often-discussed source of uncertainty. The linear Galerkin (LG) method gave smaller discretization errors on the epicardium and forward transfer errors on the body surface than the other tested methods did. These results did, however, not reflect to the Tikhonov-regularized inverse problems, unless the error was evaluated as integral over the whole epicardial surface. Overall, the choice of basis and weight functions had smaller effect on the reconstructed epicardial potential than the errors due to interpolation and insufficient modeling did.

In choosing the basis functions for boundary element computations, the error introduced by interpolation of the source data should not be overlooked. Constant basis and weight functions are spanned according to the triangles, while their linear counterparts are built around the nodes of the mesh. The results of computations are thus written in terms of triangle and node potentials, respectively. In the meshing process, nodes are commonly placed into electrode positions. If constant basis functions are used with such a mesh, the data measured with the electrodes need to be interpolated from the electrode positions to the triangles. In Publication II, the effect of such interpolation on inverse problem was studied: In optimal modeling conditions with simulated data, the interpolation increased the reconstruction error considerably. In realistic applications, however, the error due to the interpolation is probably not as large as in the optimal model, because smoothing caused by the interpolation appears to partially compensate for the modeling errors (see Figs. 4 and 5 and Section V-E in Publication II). Still, if computations can be done directly using the data at electrode positions only, there is no reason for interpolating the measured data before solving the inverse problem.

Recently, the method of fundamental solutions (MFS) was applied to the epicardial potential problem [67]. The use of MFS was motivated by listing problems of the BEM: singular integrals, difficulty of implementation, and mesh-related artifacts. For all these problems, there is, however, a solution or a work-around: The singular integral of the G operator can, with flat triangles and polynomial basis functions, be calculated analytically [22, 23]. The other singularity-related problem, the "auto-solid angle" in the discretization of the D operator [68], is not an issue in the constant methods or in the linear Galerkin method, in which the actual field computation points are inside of smooth triangles instead of being in the sharp nodes (see Publication II). Compact, general presentation of the mathematics of the epicardial potential problem (Publications II and III) and the thorough documentation of the analytical integrals in [22] coupled with the BEM library presented in Publication I enable the straightforward implementation of the BEM solver. The use of the linear Galerkin method reduces mesh-related artifacts, because computations do not need to be performed at sharp-angled nodes of the mesh.

3.2.2 Volume Conductor Modeling in Epicardial Potential Imaging

The first BEM implementation of the epicardial potential problem [26] was formulated in a homogeneous volume conductor. A formulation for a piecewise homogeneous volume conductor was reported in [69], but it has apparently not been applied to epicardial potential imaging later on. Difficulties and limitations of [69] are discussed in Publication III, in which a generalized, operator-based formulation of the problem is presented and validated. Effects of conductivity inhomogeneities on the forward epicardial potential problem have—in realistically shaped models—been studied, *e.g.*, in [69–71] and in Publication II. In the inverse epicardial potential problem, these effects have been studied in [72, 73] and in Publication II.

In [69], epicardial and body surface potential data were measured from an intact dog. Boundary element models with various simplifications were constructed, and computed surface potentials were compared to the measured ones, using the measured epicardial potentials as input data. Anisotropic thoracic muscle was approximated as suggested in [74], replacing the anisotropic layer with a scaled isotropic layer. The full model comprised the lungs, sternum, spine, and thoracic muscle layer. During sinus rhythm, this model lead to relative error (RE) of 39%. The muscle layer was found to be the most

important inhomogeneity: removing it increased the RE to 56%, while removing of all inhomogeneities gave the RE of 58%. With anterior pacing, errors were considerably larger. The effect of lungs was found insignificant. It is, however, not clear, how well these results are applicable to the human thorax; especially the structure and size of the muscle layer and the validity of the used approximation may differ.

An accurate FEM thorax model containing the lungs, anisotropic muscle layer, various fat pads, and major bones and blood vessels was built in [70]. Body surface potential maps were computed in the model containing all inhomogeneities, using a measured epicardial potential distribution. These body surface maps were then compared to corresponding maps obtained with simplified models using the same epicardial potential distribution. The anisotropic thorax muscle, subcutaneous fat, and lungs played the largest roles, causing 12–15% relative errors each.

In [71], a perfused canine heart and a homogeneous torso-shaped saline tank were used. The heart was paced from various positions, and epicardial and surface potentials were measured. The solution of the forward problem in the homogeneous volume conductor was first validated against the measured data. Then, the model geometry was altered and inhomogeneities were introduced computationally, and the effects of inhomogeneities on the tank surface potential were compared against each other. The relative difference[4] between the computed surface potentials in homogeneous and inhomogeneous models was between 7% and 17%. The conclusion was that inhomogeneities have only minor effects on the electrocardiogram.

In [70,71], the epicardial potential was assumed fixed, and differences between computed surface solutions were evaluated. Thus, the effect of the volume conductor variation on the epicardial potential was omitted. This causes errors regarding the roles of the inhomogeneities, especially those close to the heart. Overall, the role of the inhomogeneities can not be fully assessed by studying the forward problem only, because in the inverse problem, small errors in the computational model or measured data may lead to large errors in the inverse reconstruction [27].

In [72], the EDL model was used for simulation of realistic epicardial[5] and

---

[4]Relative difference is mathematically identical to the relative error, presented in Eq. 29 of Publication II

[5]In [72] and other studies of the van Oosterom group, the term "pericardial potential" is used instead of "epicardial potential".

body surface potentials in a piece-wise homogeneous volume conductor (intracardiac blood masses, lungs). Then, epicardial potentials were reconstructed utilizing a priori information of the solution. Evaluation of different volume conductor simplifications was not elaborated, but it was concluded that, in order to obtain proper results, the lungs need to be included.

The study [71] was followed by [73], in which the same measured epicardial potential patterns were used for computational generation of body surface potential maps in a piece-wise homogeneous model. Then, the inverse potential problem was solved using various model simplifications. The relative error increased by about 20 and the correlation coefficient decreased by less than 10 percentage units, when the inhomogeneities were left out. It was then concluded that modeling of the inhomogeneities can be omitted.

In Publication II, both forward and inverse problem were first solved in a homogeneous model. Then, inhomogeneities were introduced in the generation of the reference data, while the inverse reconstruction was performed using the homogeneous model. In the optimal modeling conditions (both forward and inverse transfers in identical, homogeneous models), the median relative error of the inverse reconstruction was approximately 10%. When the forward problem was solved in a model containing the lungs and the inverse reconstruction was done in a homogeneous model, the corresponding error was about 30%.

In [71,73], it was discussed that the inclusion of the inhomogeneities increases the condition number of the forward transfer matrix, leading to a more ill-posed inverse problem and thus devaluing the advantage of the more accurate transfer matrix. In Publication III, however, the condition number of the forward transfer matrix for the inhomogeneous model was smaller than that for the corresponding homogeneous model. In other words, modeling of inhomogeneities with the method described in Publication III does not increase the ill-posedness of the problem. The use of a piece-wise homogeneous thorax model instead of the homogeneous one thus prepares the way for more accurate reconstruction of epicardial potential.

3.2.3 Validation of Epicardial Potential Imaging

Major part of method development in epicardial potential imaging is based on data measured with a semi-realistic phantom: a Langendorff-perfused canine heart placed into a thorax-shaped saline tank that is equipped with surface

27

electrodes and electrode rods (see [59]). With this setup, voltages both on the surface of the tank and close to the epicardium can be recorded synchronously. Such data are ideal for developing and comparing computational methods, but the role of the inhomogeneous volume conductor and errors due to simplifications in the volume conductor model can not be directly studied. Tank studies and other validation approaches to both epicardial potential imaging and source-modeling have been reviewed, *e.g.*, in [75, 76].

Epicardial potential imaging is currently being validated with realistic human data. So far, epicardial potential imaging has been shown to localize ventricular pacing sites with accuracy of about 10 mm [64]. In comparison to electrograms measured invasively from the epicardial surface, epicardial potential imaging has been able to characterize essential features of depolarization: results in [61] suggest that earliest ventricular activation and areas of slow conduction can be localized, and that the general excitation pattern can be captured. In the same study, reconstructed electrograms were in moderately good morphological concordance with measured signals (correlation coefficient ≈ 0.7); amplitude errors were not reported. Total excitation patterns computed from epicardial potential maps have been similar to those measured earlier from isolated hearts [60].

The validation results discussed above have been obtained with homogeneous volume conductor models; inclusion of the lungs in the computational model will improve the results further.

4 Detection and Localization of Myocardial Ischemia

4.1 Myocardial Ischemia and the Electrocardiogram

Coronary artery disease leads to occlusion of coronary arteries. The occlusion causes reduction of blood supply in myocardium. The reduced blood-flow leads to disturbed hemodynamics and lack of oxygen that cause changes in electrophysiological conditions of the cardiac muscle cells. These changes alter the transmembrane potential in the ischemic region, leading thus to ECG changes. Prolonged ischemia leads to myocardial infarction, in which permanent damage for cardiac muscle cells has occurred. Myocardial infarction increases the risk of possibly lethal ventricular arrhythmias and weakens the pumping-function of the heart. [77]

Ischemic changes in the electrocardiogram are typically easiest to detect between depolarization and repolarization of the ventricular myocardium. In ECG waveforms, this plateau phase is referred to as ST segment; labeling of the ECG waveform is presented in Fig. 3. During the plateau phase, the transmembrane potential is larger in healthy myocardium than in the ischemic region. This potential-difference generates changes in the epicardial potential and electrocardiogram: Transmural ischemia causes epicardial and electrocardiographic ST potential elevation in the region overlying the ischemic area, while subendocardial ischemia may cause either ST elevation, depression, or no ST change at all [78–82]. Overall, the strength and shape of ischemic ST changes depend on the extent and severity of the ischemia, on intra- and extracellular conductivities, and on the direction of cardiac muscle fibers [78–81, 83]. The current flow and changes of epicardial potential associated with subendocardial ischemia have been characterized and visualized in [79, 80].

In addition to the ST segment, myocardial ischemia may alter also other features of the electrocardiogram, especially the QRS complex and T wave; a recent listing of electrocardiographic abnormalities that may evolve to myocardial infarction is provided in [84]. In addition, ECG markers such as QRS slope [85] and high-frequency content of the QRS complex [86] have been reported to add to the value of the ECG in diagnosis of myocardial ischemia. It has also been reported [87–89] that electrodes outside the standard 12-lead setup improve the electrocardiographic detection of myocardial

ischemia. In [87, 88], the optimal unipolar [88] or bipolar leads [87] for detecting ischemia were derived by searching for the largest [87] or statistically most significant [88] alterations in ST60 (see Fig. 3) body surface potential maps measured during induced ischemia. The electrode layouts suggested in [87, 88] were applied in Publication IV.

In Publications IV–VI, both ST potentials and other linear ECG markers are used in detection, localization, and size quantification of myocardial ischemia, applying dipole modeling and epicardial potential imaging. To the author's knowledge, dipole modeling has not been used before in quantitative analysis of the myocardial ischemia. In Dalhousie university, the ischemic electrocardiogram has been studied using a measurement system and dataset very similar to ours; epicardial potential imaging has been applied to characterization of ischemia in, *e.g.*, [63, 90].

4.2 Datasets and Preprocessing

The datasets used in Publications IV–VI were collected in Division of Cardiology at Helsinki University Central Hospital. Body surface potential mapping was performed using BioSemi Mark VI and Active Two amplifiers[6] and strip electrodes. The measurement system is described in [91], and the electrode layout is visualized in Fig. 4a of this text and in Fig. 1 of Publication IV.

In percutaneous transluminal coronary angioplasty (PTCA), a catheter with an inflatable balloon is inserted into the occluded coronary artery, and the artery is re-opened by inflating the balloon at the occlusion site [92]. During the inflation, the artery is totally blocked, leading to temporary supply ischemia. PTCA provides an idealized model of the ischemic myocardium: the site of the occlusion is known, and the artery is totally blocked.

In the first dataset ("the PTCA set"), the BSPM was measured in the catheter laboratory during scheduled PTCA operations in 22 patients. The angioplasty was performed in left anterior descending (LAD, $n = 8$), left circumflex (LCX, $n = 7$), or right coronary artery (RCA, $n = 7$). Typical coronary artery anatomy is visualized in Fig. 2. This dataset was used in Publications IV and VI. BSPM data measured during PTCA were also used in [63, 87, 88, 90]; the electrode layout was nearly identical to that in our studies.

---

[6]http://www.biosemi.com

30

The second dataset contains BSPM data from 84 healthy volunteers and 79 patients suffering from acute myocardial ischemia ("the acute set"). The measurements were carried out in the coronary care unit within 12 hours from the onset of symptoms. The inclusion criteria for the set were chest pain and either alterations in the 12-lead ECG suggestive of myocardial ischemia or elevation of myocardial enzymes or both. The patients were grouped according to the culprit coronary artery and presence of acute myocardial infarction (AMI). The culprit artery was specified in coronary angiography, and the AMI grouping was done according to the CK–Mb (creatine kinase–Mb) mass maximum. This dataset was used in Publication V.

The data were pre-processed semi-automatically: a 50-Hz filter was applied when necessary, the baseline-wandering was corrected with a third-order spline function, ectopic beats were rejected, and the data were signal-averaged [94]. The selective averaging was in the PTCA set computed over 11 beats and in the acute set over the whole measurement. Channels with bad signal quality were interpolated using the surface Laplacian [95]. A pre-processed ECG signal is presented in Fig. 3.

The fiducial time-points were detected automatically from the averaged ECG signals: The QRS onset and offset times were defined from the vector magnitude of the high-pass-filtered signals using envelopes. The apex and end of the T wave were defined for all signals as described in [94]; in further analysis, the median of these channel-specific time instants was used. On basis of the averaged data and the fiducial time points, various linear ECG markers were extracted. The markers contained both instantaneous maps and integral maps over various parts of the QRS complex, ST segment, and T wave.
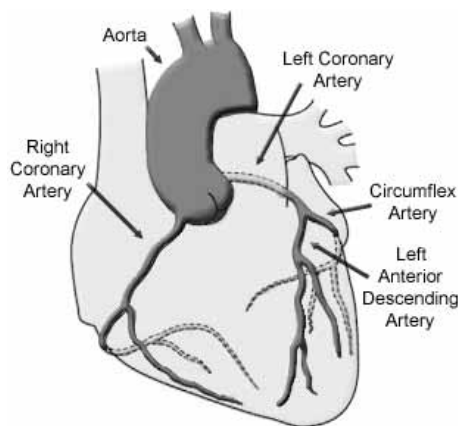

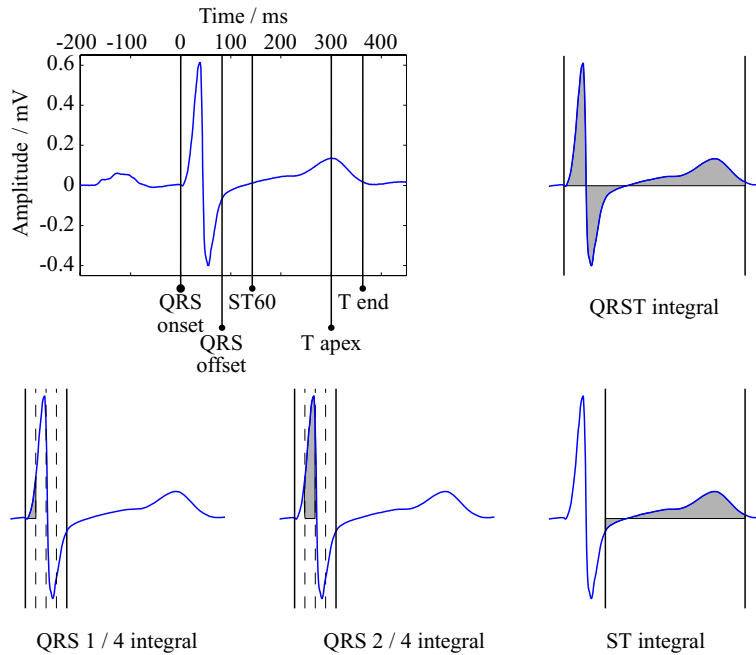Figure 2: *Coronary anatomy, modified from [93]*

31

Figure 3: *A preprocessed ECG signal with fiducial time-points, ST60 time-instant, and various integral markers. The QRS complex is the period between the QRS onset and offset, and the ST segment starts from the QRS offset and continues as the T wave. The T wave onset-point was not defined or used in this study.*

The fiducial time points and some of these markers are illustrated in Fig. 3. For the PTCA set, delta maps [87] were generated by subtracting the map before the balloon inflation from the map with maximal ST changes. The delta maps thus represent only the ECG alterations caused by the balloon.

4.3 Dipole Modeling

In Publications IV and V, dipole modeling is applied in spatial characterization of measured electrocardiograms. While both studies deal with ischemic hearts, aims and methods are different: In Publication IV, the aim is to classify the ischemic electrocardiogram according to the coronary artery experiencing reduced flow, and the classification is based on angles between dipoles. In Publication V, it is studied, whether simple parameters derived from dipoles are able to discriminate patients from controls and predict the extent of the resulting infarction as measured by creatine kinase–Mb enzyme.

These discriminating or predicting parameters include, *e.g.*, amplitudes of orthogonal components or projections of the dipole.

The dipole hypothesis in these studies originated from dipolar patterns observed in body surface potential maps (see Fig. 2 in Publication IV). The aim was not to localize the source of the abnormal cardiac electrical activity with help of the dipolar source model. Instead, the dipole was used as a tool for characterizing the morphology of the body surface potential distribution (see also Section 3.1.2).

4.3.1 PTCA Set (Publication IV)

In the PTCA delta maps presented in [87], the population-average maps of the ST60 potential[7] show dipolar morphology, and the map orientation depends on the occluded artery. In our PTCA set, the corresponding maps were very similar to those in [87]. In Publication IV it was studied, whether the map orientation can be characterized with a dipole model, and whether the resulting dipoles can be used for discriminating between culprit arteries. The ST60 population-average maps and corresponding dipoles of our PTCA set are visualized in Figs. 2 and 3 of Publication IV.

Computation of the equivalent current dipoles was performed as described in Publications IV and V using the development version of the BEM library presented in Publication I. The dipole position was either optimized for the best reconstruction of the measured data in each patient ("best-reconstructing"), pre-fixed, or defined from the population average maps ("artery-specific").

In all patients, the Dalhousie thorax model [17] was used; variation in patient anatomy and electrode positioning was omitted. The thorax model was assumed otherwise homogeneous, but the anisotropic thoracic muscle layer was approximated as suggested in [1, 74], replacing the anisotropic layer with a scaled isotropic layer. When this volume expansion method was applied, the dipoles fitted to the dataset had, according to visual inspection, smaller variation than in the fully homogeneous model. In the first classification tests, the volume-expanded model also performed better than the homogeneous one. All further analysis was thus done with the expanded model.

In addition to the full BSPM set, five reduced electrode-sets were applied: those of the 12- and 18-lead [89] ECGs, a custom set modified from the 12-

---

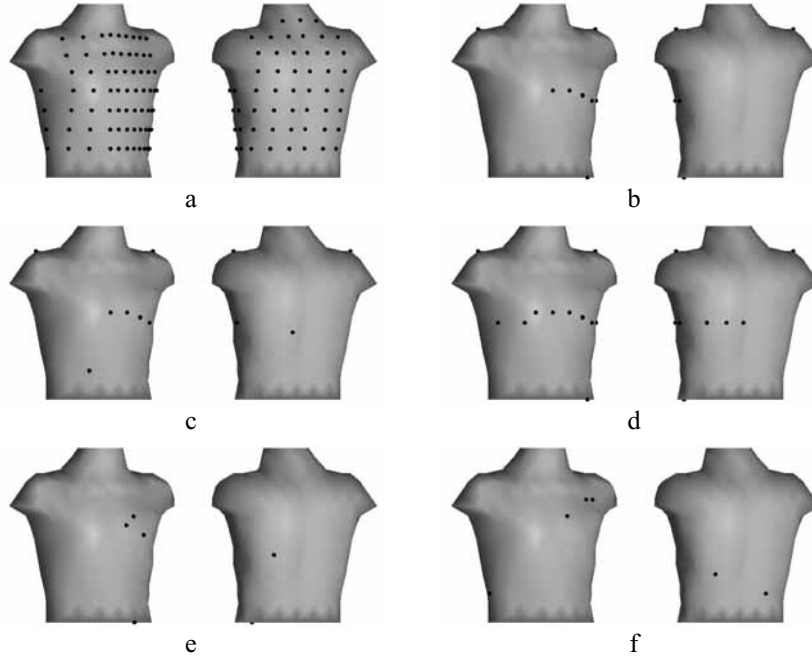[7]ST60 potential = potential 60 ms after the QRS offset

Figure 4: *Electrode setups used for ischemia classification. a) BSPM, b) 12-lead, c) modified 12-lead, d) 18-lead [89], e) Horáček [87], and f) Kornreich [88].*

lead set ("modified 12-lead"), and the 5-electrode sets proposed in [87, 88]. Although the datasets and principles of discrimination in [87,88] were similar to those used in this Thesis, there is an essential difference: in [87, 88], the best electrode positions for a given ECG marker were sought for, whereas in the dipole studies of this Thesis, the main spatial features of potential distribution sampled by a given electrode-set are distilled into one dipole, which is then used for classification.

The electrode layouts of the applied electrode-sets are visualized in Fig. 4. The reduced-set data were generated from the BSPM markers; to enable field calculation in the 12- and 18-lead sets, the limb electrodes were positioned on shoulders and left hip and the chest electrodes were placed in the best-matching nodes of the thorax model. ECG markers at positions that did not match with the electrodes of the BSPM set were interpolated using the surface Laplacian [95].

Patients were classified by comparing the dipole moment computed from the test case ("test dipole") to the corresponding dipole moments computed

from the population average maps of other patients in leave-one-out manner: the test dipole was always independent on the data used for obtaining the population average maps. The cosine of the angle between the dipoles was chosen as the classification parameter. When reduced electrode-sets were used, the population average maps were constructed with both BSPM and the set in question. After preliminary testing, only the ST60 potential was used in classification.

With the BSPM set, 21 of the 22 patients were classified correctly using any dipole positioning. When reduced sets were used, the pre-fixed or artery-specific dipole positions performed better than the best-reconstructing dipole did. The modified 12-lead set performed as well as the BSPM, and the 5-electrode set of [87] was able to classify 20 patients correctly. The 12-lead set provided the correct classification in 18 cases, while the 18-lead set succeeded in either 19 or 20 cases. The 5-electrode system suggested in [88] seems to be badly suitable for use with dipole modeling. With reduced electrode-sets and artery-specific dipoles, the positions defined according to the BSPM data performed better than those defined with the set being tested.

These results show that dipole modeling is a powerful tool for characterizing the orientation of body surface potential maps. The method presented here is applicable also with reduced electrode-sets, especially when the dipole positions are pre-fixed according to prior BSPM results. In addition to the quantitative information obtained from the dipoles, the use of the dipole model provides a way for visualizing the heart vector, thus facilitating the manual interpretation of the electrocardiogram.

4.3.2   Acute Set (Publication V)

In Publication V, dipole modeling was used for detection of myocardial ischemia and size quantification of the resulting myocardial infarction. The dataset was subdivided according to the culprit coronary artery and presence of myocardial infarction, resulting in eight patient categories (see Table 2 in Publication V). The field computation was done with the same model as in Publication IV, and the dipole position was either the pre-fixed or best-reconstructing one.

First, dipoles were fitted to all BPSM markers resulting from the preprocessing, using either the full BSPM set or the electrode set of the reconstructed 12-lead ECG. Next, 10 parameters were extracted from each dipole. Then,
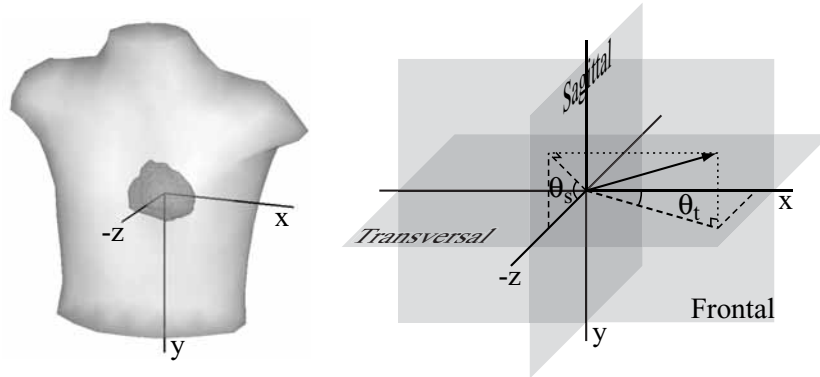
Figure 5: *The Dalhousie thorax model, its principal axes, and projection surfaces. In addition, transversal θ_t and sagittal θ_s projection angles are presented.*

the ability of each dipole parameter to discriminate between patient groups and controls was assessed in leave-one-out manner, resulting in estimates of sensitivity and specificity. The size quantification was carried out by finding the best correlation coefficient between the dipole markers and CK-Mb mass maximum [96]. The statistical reliability of the correlations was assessed with confidence interval (CI), computed non-parametrically using the bias-corrected accelerated bootstrap [97,98]. The dipole parameters are described in Section 2.4 of Publication V, and the projection planes and angles used in the parameter definitions are illustrated in Fig. 5.

When the best-reconstructing dipoles and BSPM were used, the first and second QRS-quarter integrals performed best with left coronary arteries, while the T apex potential was the best-discriminating ECG marker in artery-unspecific patient categories (see Table 2 in Publication V). When the pre-fixed dipole position was used with the BSPM set, the discrimination performance was slightly better than in case of the best-reconstructing dipoles. With the 12-lead set, only the pre-fixed dipole position was used. The first QRS-quarter integral discriminated best with LAD infarctions; in other groups, the best performance was obtained with repolarization-characterizing markers (see Table 3 in Publication V). All dipole parameter categories except the total dipole amplitude were represented in the results; in general, the amplitudes and directional cosines of the dipole projections stand above the crowd. Overall, the discrimination performance of the 12-lead set was slightly better than that of the BSPM set. These results are discussed further in Section 4 of Publication V.

36

Table 3: *Best parameters for the size quantification of myocardial infarction using the 12-lead electrode set with the pre-fixed dipole position; R is the correlation coefficient and CI its confidence interval, "int." labels integral markers, "T apex" is the median amplitude of the T wave, and "QRS 2 / 4" is the second quarter of the QRS.*

Group	n	Marker	D. Para	R	CI
All12	79	QRS 2 / 4 int.	$\cos\theta_t$	-0.59	$[-0.79, -0.27]$
LAD12	32	QRS 2 / 4 int.	$\cos\theta_t$	-0.91	$[-0.95, -0.83]$
LCX12	10	QRST int.	$\cos\theta_t$	-0.85	$[-0.98, -0.57]$
RCA12	26	T apex.	Q_y	-0.38	$[-0.69, -0.03]$
AMI12	68	QRS 2 / 4 int.	$\cos\theta_t$	-0.57	$[-0.78, -0.23]$
AMI12LAD	28	QRS 2 / 4 int.	$\cos\theta_t$	-0.90	$[-0.95, -0.81]$
AMI12LCX	8	QRST int	$\cos\theta_t$	-0.79	$[-0.96, 0.02]$
AMI12RCA	22	S40 int.	$\cos\theta_s$	-0.43	$[-0.66, -0.10]$

The correlations presented in Publication V were calculated from the BSPM set using the best-reconstructing dipoles. Corresponding parameters for the 12-lead electrode set with the pre-fixed dipole position are presented in Table 3. In artery-unspecific and LAD patient groups, the cosine of the transversal projection angle calculated from the integral over the second QRS-quarter shows a strong correlation with the CK-Mb.

4.4 Epicardial Potential Imaging

In Publication VI, epicardial potential imaging was applied in localization of the ischemic region from body surface potential maps. The localization was done by searching for the ischemia-characteristic region of altered epicardial potential in the ST60 delta maps of the PTCA dataset. The same dataset was used in Publication IV for classification of the ischemia according to the culprit artery with help of dipole models; see Section 4.3.1.

While the aim in these two PTCA applications is partially the same, the methodologies are different: In Publication IV, the dipole-hypothesis was based on geometrical differences of the body surface maps, and the classification was done by comparing each patient to all patient groups, without any reference to cardiac anatomy. In Publication VI, the hypothesis was based on known features of typical ischemic epicardial potentials and elec-

trocardiograms, and the results were visualized on an anatomical model of the epicardium; no quantitative classification was done. The PTCA dipole study is thus a combination of feature extraction and classification, while this epicardial potential imaging study essentially deals with functional imaging with simple a priori conditions.

Epicardial potential imaging was carried out using the homogeneous Dalhousie thorax model that was used also in most of the computations of Publication II. Field computations were carried out with the constant collocation (CC) method, and the single-layer integrals were computed numerically—these were for the authors the only methods implemented at that time. Regularization was done with Tikhonov's second-order method, following guidelines of [17]. In order to use this "traditional method", the delta maps had to be interpolated from nodal electrode positions to the centroids of all triangles. The interpolation was carried out with the surface Laplacian method [95].

First, the traditional method was applied to the dataset. The regularization parameter was chosen manually so that the goodness of fit[8]between the source data and the reconstructed surface potential was approximately 0.96. The resulting epicardial potential maps, presented in Figs. 3a–5a of Publication VI, were not satisfactory: instead of showing a well-defined positive region above the ischemic region, the maps were fragmented, containing many positive and negative regions and strong gradients.

To provide for smoother solutions and a more compact transfer matrix, a nodal approach was developed. In this approach, unit potentials defined in nodes were first interpolated to triangle centroids using the surface Laplacian. Then, the transfer matrix for these interpolated unit potentials was constructed by applying CC-discretized Eq. 42, and the resulting body surface potentials were interpolated to nodes. The use of interpolation provides for spatially smoother basis for the epicardial potential: instead of the standard constant basis functions (non-overlapping, defined in single triangles), each basis function in the nodal approach spans over several triangles. The inverse reconstructions obtained with this "lead-field" method were—at the same goodness of fit—considerably smoother than those obtained with the traditional method (see Figs. 3–5 in Publication VI).

In [63], the volume conductor model consisted of the Dalhousie thorax surface and an epicardial surface that was more coarse than the one used in our study. Field computations were done with linear collocation method, and the inverse

---

[8]See Eq. 7 of Publication V; in Eq. 8 of Publication VI there is an error.

transfer matrix was constructed with help of the Tikhonov regularization, in which the regularization parameter was set with help of simulated data. The analysis was carried out using delta maps constructed from ST integral maps. Results were, according to visual comparison, slightly more detailed than those obtained with the lead-field method in our study, but much smoother than those resulting from the traditional method.

While the lead-field method and the method applied in [63] are able to yield smooth epicardial potential maps that reflect geometrical features of the body surface potential maps, they may, due to modeling errors or under- or over-regularization, fail in giving a clear estimate on the location and extent of the ischemic region. In order to provide for an easy-to-interpret, robust tool for localization of the ischemic region, another method was developed. In this "template method", the epicardial potential around each node of the epicardial mesh is modeled with help of a pre-specified neighborhood function. From these template epicardial potential maps, corresponding body surface potential maps are computed and used for iterative searching of the template that best fits the measured data.

Results obtained with the template method are, for representative cases, displayed in Figs. 3c–5c and Fig. 6 of Publication VI. The template method produced morphologically simple maps, in which the elevated epicardial potential was close to the location of the map maximum suggested by the lead-field method. In the whole patient set, the localizations suggested by the best-fitting templates were anatomically logical: they were always in the region that is typically perfused by the same coronary artery that was blocked during the BSPM measurement, with only a slight overlap between different patient categories.

After implementing the linear collocation (LC) and Galerkin (LG) methods and analytical integrals for the epicardial potential problem, they were also tested with the PTCA set—also with lungs included in the model. In visual comparison, reconstructions obtained with the homogeneous model and LC or LG methods were morphologically similar to, while slightly more detailed than, those obtained with the lead-field method. Correlation coefficients for the LG and lead-field reconstructions were between 97% and 99%. The lead field method thus reconstructed the main spatial characteristics of the myocardial ischemia as well as the LC and LG methods did. Relative differences ranged between 16% and 37%.

Next, the role of the lungs in reconstruction of the epicardial potential was
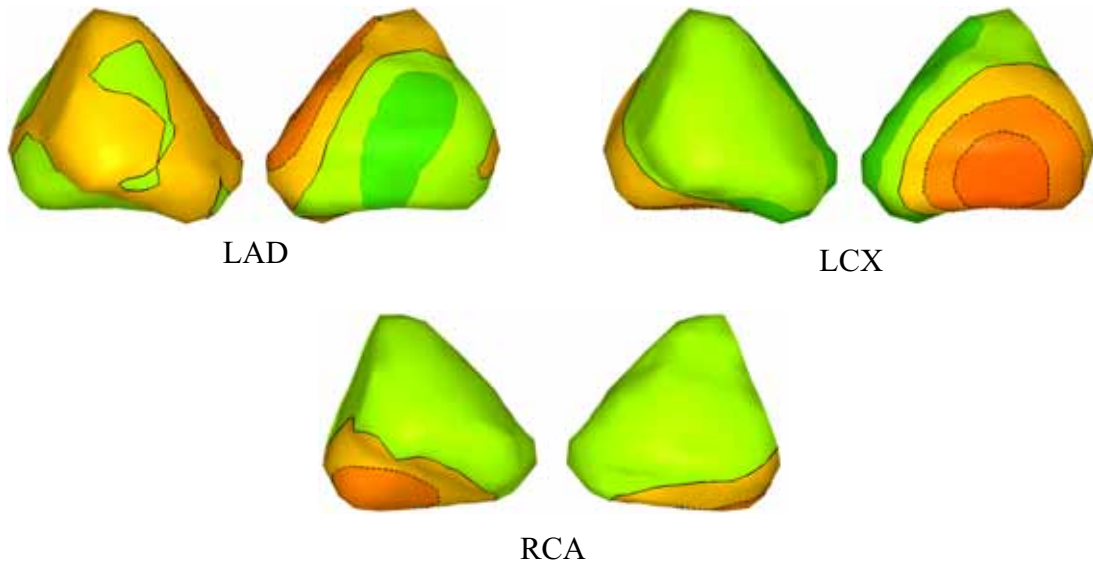
Figure 6: *Epicardial potentials map reconstructed from PTCA difference maps using the linear Galerkin method in a volume conductor model containing the lungs; contour step is 50 μV, and positive contours are marked with dashed line.*

assessed with the LG method. The inclusion of the lungs in the model increased the amplitudes and added some detail to the maps, but main spatial features did not change; correlation coefficients were between 93% and 98% and relative differences between 25% and 39%. Epicardial potential maps of the representative cases obtained with the lungs included in the model are visualized in Fig. 6.

Finally, the template method was applied with the LG transfer matrices. In the homogeneous model, the results similar to those in Publication VI were obtained; in some of the patients the localizations changed, but the general pattern remained the same. When the lungs were included, localizations moved, on average, slightly further away from the apical tip, and the separation between the patient categories was improved. The new template localizations are displayed in Fig. 7. These results suggest that inclusion of the lungs improves the results also in applications, in which patient-specific models are not used or the inverse problem is solved with simple, coarse methods.
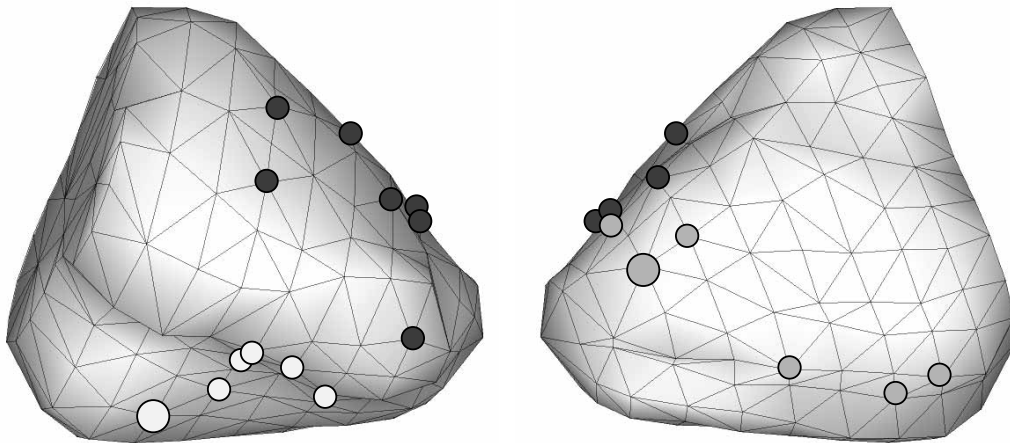
Figure 7: *Centers of ischemic regions for all LAD, LCX, and RCA patients marked with dark, medium, and light gray circles, respectively*

5 Summary and Outlook

In this Thesis, methods for solving the forward and inverse problems of electrocardiography were developed and applied to characterization of acute myocardial ischemia.

Basic methods for solving quasi-static potential-problems using the BEM were collected to a Matlab toolbox. This Helsinki BEM library has been succesful; it is currently in use in over 20 foreign research groups. In addition to electrocardiographic problems, the methods in the library can be applied directly to, *e.g.*, electro- and magnetoencephalography, magnetocardiography, and electrostatic scattering. For the author, structures and routines of the library have given a solid foundation for further method development.

Compared to conventionally used collocation methods, the linear Galerkin (LG) method was found to produce smaller forward-transfer and discretization errors in the epicardial potential problem. A good inverse solution needs an accurate forward solution as prerequisite; the use of the linear Galerkin method instead of the collocation method is thus, in general, recommended. But, when the inverse problem was solved using the traditional Tikhonov regularization, the LG method was, overall, not better than the other methods. In most applications of epicardial potential imaging, the lungs have been omitted from the thoracic volume conductor model. If such a simplification is done, the choice of basis and weighting functions is insignificant. The transfer matrix derived in this Thesis enables the inclusion of lungs in an easy-to-implement manner, without increasing the ill-posedness of the problem. The quest for the accurate reconstruction of the epicardial potential should thus head towards more accurate volume conductor models and more advanced regularization techniques. The methodology developed in this Thesis can also be applied to reconstruction of cortical potential distribution from electroencephalographic data.

In the practical part of this Thesis, dipole modeling and epicardial potential imaging were applied to detection, quantification, and localization of acute myocardial ischemia. The results show that dipole modeling is an effective tool for extracting main geometrical features from the body surface potential maps or from conventional ECG recordings: 21 of the 22 PTCA patients were classified correctly using the BSPM set, and 20 patients with a 5-electrode set described elsewhere. Dipole-markers gave also encouraging results in detection and quantification of acute ischemia in a set of 79 patients and 84 controls. Epicardial potential imaging characterized effectively the morpho-

logical features of the PTCA delta maps. The simple and robust template method, developed in this Thesis, was able to localize the ischemic regions anatomically correctly, although patient-specific volume conductor models were not used.

The method development carried out in this Thesis prepares the way for more accurate inverse reconstructions of epicardial potential. The results obtained with clinical datasets show that the modeling-approach can provide valuable information also without patient-specific models and complicated protocols.

References

[1] R.M. Gulrajani. *Bioelectricity and Biomagnetism*. Wiley and Sons, 1998.

[2] P.W. MacFarlane. Lead systems. In P.W. MacFarlane and T.D.V. Lawrie, editors, *Comprehensive Electrocardiography*, pages 315–352. Pergamon Press, 1989.

[3] J.D. Jackson. *Classical Electrodynamics*. Wiley and Sons, 3rd edition, 1999.

[4] R. Plonsey and D. Heppner. Considerations of quasistationarity in electrophysiological systems. *Bull. Math. Biophys*, 29:657–664, 1967.

[5] H.P. Schwan and C.F. Kay. Specific resistance of body tissues. *Circ. Res.*, 4:664–670, 1956.

[6] H.C. Burger and R. van Dongen. Specific resistivity of body tissues. *Phys. Med. Biol.*, 4:431–447, 1961.

[7] S. Rush, J.A. Abildskov, and R. McFee. Resistivity of body tissues at low frequencies. *Circ. Res.*, 12:40–50, 1963.

[8] S. Gabriel, R. W. Lau, and C. Gabriel. The dielectric properties of biological tissues: II. Measurements in the frequency range 10 Hz to 20 GHz. *Phys. Med. Biol.*, 41:2251–2269, 1996.

[9] H.P. Schwan and C.F. Kay. Capacitive properties of body tissues. *Circ. Res.*, 5:439–443, 1957.

[10] H.P. Schwan and C.F. Kay. The conductivity of living tissues. *Ann. N.Y. Acad. Sci.*, 65:1007–1013, 1957.

[11] M. Stenroos. *Electrocardiographic Characterization of Myocardial Ischemia with Numerical Field Calculation*. Licentiate thesis, Helsinki University of Technology, 2005.

[12] J.G. Stinstra and M.J. Peters. The volume conductor may act as a temporal filter on the ECG and EEG. *Med. Biol. Eng. Comp.*, 36:711–716, 1998.

[13] C.A. Brebbia and J. Dominguez. *Boundary Elements: an Introductory Course*. McGraw–Hill, 1989.

[14] A.C.L. Barnard, I.M. Duck, and M.S. Lynn. The application of electromagnetic theory to electrocardiology. I. Derivation of the integral equations. *Biophys. J.*, 7:443–462, 1967.

[15] A.C.L. Barnard, I.M. Duck, M.S. Lynn, and W.P. Timlake. The application of electromagnetic theory in electrocardiology. II. Numerical solution of the integral equations. *Biophys. J.*, 7:463–490, 1967.

[16] N. Morita, N. Kumagai, and J.R. Mautz. *Integral Equation Methods for Electromagnetics*, pages 134–135. Artech House, 1990.

[17] B.M. Horáček and J.C. Clements. The inverse problem of electrocardiography: A solution in terms of single- and double-layer sources on the epicardial surface. *Math. Biosci.*, 144:119–154, 1997.

[18] B.M. Horáček. *The Effect on Electrocardiographic Lead Vectors of Conductivity Inhomogeneities in the Human Torso*. PhD thesis, Dalhousie University, 1971.

[19] D.B. Geselowitz. On bioelectric potentials in an inhomogeneous volume conductor. *Biophys. J.*, 7:1–11, 1967.

[20] A. van Oosterom and J. Strackee. The solid angle of a plane triangle. *IEEE Trans. Biomed. Eng.*, BME-30:125–126, 1983.

[21] J.C. de Munck. A linear discretization of the volume conductor boundary integral equation using analytically integrated elements. *IEEE Trans. Biomed. Eng.*, 39:986–989, 1992.

[22] R.D. Graglia. On the numerical integration of the linear shape functions times the 3-D Green's function or its gradient on a plane triangle. *IEEE Trans. Antennas Propag.*, 41:1448–1455, 1993.

[23] S. Järvenpää, M. Taskinen, and P. Ylä-Oijala. Singularity extraction technique for integral equations with higher order basis functions on plane triangles and tetrahedra. *Int. J. Numer. Meth. Eng.*, 58:1149–1165, 2003.

[24] M.S. Lynn and W.P. Timlake. The use of multiple deflations in the numerical solution of singular systems of equations, with applications to potential theory. *SIAM J. Num. Anal.*, 5:303–322, 1968.

[25] G. Fischer, B. Tilg, F. Hanser, B. Messnarz, and P. Wach. On modeling the Wilson terminal in the boundary and finite element method. *IEEE Trans. Biomed. Eng.*, 49:217–224, 2002.

[26] R.C. Barr, M. Ramsey, and M.S. Spach. Relating epicardial to body surface potential distributions by means of transfer coefficients based on geometry measurements. *IEEE Trans. Biomed. Eng.*, BME-24:1–11, 1977.

[27] F. Greensite. Heart surface electrocardiographic inverse solutions. In Bin He, editor, *Modeling and Imaging of Bioelectrical Activity: Principles and Applications*, pages 119–160. Kluwer Academic, 2004.

[28] H. Helmholtz. Ueber einige Gesetze der Vertheilung elektrischer Ströme in körperlichen Leitern mit Anwendung auf die thierisch-elektrischen Versuche. *Annalen der Physik und Chemie*, 89:211–233; 353–377, 1853.

[29] J.T. Nenonen, M.S. Hämäläinen, and R.J. Ilmoniemi. Minimum-norm estimation in a boundary-element torso model. *Med. Biol. Eng. Comput.*, 32:43–48, 1994.

[30] W. Einthoven, G. Fahr, and A. de Waart. Über die Richtung und die manifeste Grösse der Potentialschwankungen in menschlichen Herzen und über den Einfluss der Herzlage auf die Form des Elektrokardiogramms. *Pflügers Archivs für Physiologie*, 150:275–315, 1913.

[31] H.C. Burger and J.B. van Milaan. Heart-vector and leads. *Brit. Heart. J.*, 8:157–161, 1946.

[32] H.C. Burger and J.B. van Milaan. Heart-vector and leads: Part II. *Brit. Heart J.*, 9:154–160, 1947.

[33] H.C. Burger and J.B. van Milaan. Heart-vector and leads: Part III. *Brit. Heart J.*, 10:229–233, 1948.

[34] B. Taccardi. Distribution of heart potentials on the thoracic surface of normal human subjects. *Circ. Res.*, 12:341–352, 1963.

[35] E. Frank. An accurate, clinically practical system for spatial vectorcardiography. *Circulation*, 13:737–749, 1956.

[36] R.E. Ideker, J.P. Bandura, R.A. Larsen, J.W. Cox, F.W. Keller, and D.A. Brody. Localization of heart vectors produced by epicardial burns and ectopic stimuli; validation of a dipole ranging method. *Circ. Res.*, 36:105–112, 1975.

[37] R.E. Ideker, J.P. Bandura, J.W. Cox, F.W. Keller, D.M. Mirvis, and D.A. Brody. Path and significance of heart vector migration during

QRS and ST–T complexes of ectopic beats in isolated perfused rabbit hearts. *Circ. Res.*, 41:558–564, 1977.

[38] P. Savard, F.A. Roberge, J.B. Perry, and R.A. Nadeau. Representation of cardiac electrical activity by a moving dipole for normal and ectopic beats in the intact dog. *Circ. Res.*, 46:415–425, 1980.

[39] D.M. Mirvis and M.A. Holbrook. Body surface distributions of repolarization potentials after acute myocardial infarction. III. Dipole ranging in normal subjects and in patients with acute myocardial infarction. *J. Electrocardiol.*, 14:387–398, 1981.

[40] R.M. Gulrajani, H. Pham-Huy, R.A. Nadeau, P. Savard, J. de Guise, R.E. Primeau, and F.A. Roberge. Application of the single moving dipole inverse solution to the study of the Wolff–Parkinson–White syndrome in man. *J. Electrocardiol.*, 17:271–287, 1984.

[41] T.F. Oostendorp and A. van Oosterom. Source parameter estimation in inhomogeneous volume conductors of arbitrary shape. *IEEE Trans. Biomed. Eng.*, 36:382–391, 1989.

[42] K. Pesola, J. Nenonen, R. Fenici, J. Lötjönen, M. Mäkijärvi, P. Fenici, P. Korhonen, K. Lauerma, M. Valkonen, L. Toivonen, and T. Katila. Bioelectromagnetic localization of a pacing catheter in the heart. *Phys. Med. Biol*, 44:2565–2578, 1999.

[43] A.A. Armoundas, A.B. Feldman, R. Mukkamala, B. He, T.J. Mullen, P.A. Belk, Y.Z. Lee, and R.J. Cohen. Statistical accuracy of a moving equivalent dipole method to identify sites of origin of cardiac electric activation. *IEEE Trans. Biomed. Eng.*, 50:1360–1370, 2003.

[44] Y. Fukuoka, T.F. Oostendorp, D.A. Sherman, and A.A. Armoundas. Applicability of the single equivalent moving dipole model in an infinite homogeneous medium to identify cardiac electrical sources: A computer simulation study in a realistic anatomic geometry torso model. *IEEE Trans. Biomed. Eng.*, 53:2436–2444, 2006.

[45] M.E. Barley, A.A. Armoundas, K.J. Choppy, A.M Galea, G.B. Hirschmann, and R.J. Cohen. Demonstration of a novel catheter guiding method for the ablative therapy of ventricular tachycardia. *Comput. Cardiol. 2006*, 33:613–616, 2006.

[46] D. Gabor and C.V. Nelson. Determination of the resultant dipole of the heart from measurements on the body surface. *J. Appl. Phys*, 25:413–416, 1954.

[47] J. Nenonen, T. Katila, M. Leiniö, J. Montonen, M. Mäkijärvi, and P. Siltanen. Magnetocardiographic functional localization using current multipole models. *IEEE Trans. Biomed. Eng.*, 38:648–657, 1991.

[48] R.M. Gulrajani, P. Savard, and F.A. Roberge. The inverse problem in electrocardiology: solutions in terms of equivalent sources. *Crit. Rev. Biomed. Eng.*, 16:171–214, 1988.

[49] J. Nenonen, K. Pesola, H. Hänninen, K. Lauerma, P. Takala, T. Mäkelä, M. Mäkijärvi, J. Knuuti, L. Toivonen, and T. Katila. Current-density estimation of exercise-induced ischemia in patients with multivessel coronary artery disease. *J. Electrocardiol.*, 34 Suppl.:37–42, 2001.

[50] G. Huiskamp and A. van Oosterom. The depolarization sequence of the human heart surface computed from measured body surface potentials. *IEEE Trans. Biomed. Eng.*, 35:1047–1058, 1988.

[51] D.B. Geselowitz. On the theory of the electrocardiogram. *Proceedings of the IEEE*, 77:857–876, 1989.

[52] A. van Oosterom. Genesis of the T wave as based on an equivalent surface source model. *J. Electrocardiol.*, 36 Suppl.:217–227, 2001.

[53] A. van Oosterom and T.F. Oostendorp. ECGSIM: an interactive tool for studying the genesis of QRST waveforms. *Heart*, 90:165–168, 2004.

[54] D.B. Geselowitz and W.T. Miller III. A bidomain model for anisotropic cardiac muscle. *Ann. Biomed. Eng.*, 11:191–206, 1983.

[55] T. Berger, G. Fischer, B. Pfeifer, R. Modre, F. Hanser, T. Trieb, F.X. Roithinger, M. Stühlinger, O. Pachinger, B. Tilg, and F. Hintringer. Single-beat noninvasive imaging of cardiac electrophysiology of ventricular pre-excitation. *J. Amer. Coll. Cardiol.*, 48:2045–2054, 2006.

[56] R. Modre, B. Tilg, G. Fischer, F. Hanser, B. Messnarz, M. Seger, F. Hintringer, and F.X. Roithinger. Ventricular surface activation time imaging from electrocardiogram mapping data. *Med. Biol. Eng. Comput.*, 42:146–150, 2004.

[57] B. Tilg, G. Fischer R. Modre, F. Hanser, B. Messnarz, and F.X. Roithinger. Electrocardiographic imaging of atrial and ventricular electrical activation. *Med. Imag. Anal.*, 7:391–398, 2003.

[58] R. Modre, B. Tilg, G. Fischer, F. Hanser, B. Messnarz, M. Seger, M.F.H. Schocke, T. Berger, F. Hintringer, and F.X. Roithinger. Atrial noninvasive activation mapping of paced rhythm data. *J. Cardiovasc. Electrophysiol.*, 14:1–8, 2003.

[59] H.S. Oster, B. Taccardi, R.L. Lux, P.R. Ershler, and Y. Rudy. Noninvasive electrocardiographic imaging: Reconstruction of epicardial potentials, electrograms, and isochrones and localization of single and multiple electrocardiac events. *Circulation*, 96:1012–1024, 1997.

[60] C. Ramanathan, R.N. Ghanem, P. Jia, K. Ryu, and Y. Rudy. Noninvasive electrocardiographic imaging for cardiac electrophysiology and arrhythmia. *Nature Med.*, 10:422–428, 2004.

[61] R.N. Ghanem, P. Jia, C. Ramanathan, K. Ruy, A. Markowitz, and Y. Rudy. Noninvasive electrocardiographic imaging (ECGI): Comparison to intraoperative mapping in patients. *Heart Rhythm*, 2:339–354, 2005.

[62] Y. Rudy and B.J. Messinger-Rapport. The inverse problem in electrocardiography: Solutions on Terms of Epicardial Potentials. *CRC Crit. Rev. Biomed. Eng.*, 16:215–268, 1988.

[63] R.S. MacLeod, M. Gardner, R.M. Miller, and B.M. Horáček. Application of an electrocardiographic inverse solution to localize ischemia during coronary angioplasty. *J. Cardiovasc. Electrophysiol.*, 6:2–18, 1995.

[64] S. Ghosh and Y. Rudy. Accuracy of quadratic versus linear interpolation in noninvasive electrocardiographic imaging (ECGI). *Ann. Biomed. Eng*, 33:1187–1201, 2005.

[65] P. Colli-Franzone, L. Guerri, S. Tentoni, C. Viganotti, S. Baruffi, S. Spaggiari, and B. Taccardi. A mathematical procedure for solving the inverse potential problem of electrocardiography. Analysis of the time–space accuracy from in vitro experimental data. *Math. Biosci.*, 77:353–396, 1984.

[66] A. Pullan. A high-order coupled finite element/boundary element torso model. *IEEE Trans. Biomed. Eng.*, 43:292–298, 1996.

[67] Y. Wang and Y. Rudy. Application of the method of fundamental solutions to potential-based inverse electrocardiography. *Ann. Biomed. Eng*, 34:1272–1288, 2006.

[68] A.S. Ferguson and G. Stroink. Factors affecting the accuracy of the boundary element method in the forward problem I: Calculating the surface potentials. *IEEE Trans. Biomed. Eng.*, 44:1139–1155, 1997.

[69] P.C. Stanley, T.C. Pilkington, and M.N. Morrow. The effects of thoracic inhomogeneities on the relationship between epicardial and torso potential. *IEEE Trans. Biomed. Eng*, BME-33:273–284, 1986.

[70] R.N. Klepfer, C.R. Johnson, and R.S. MacLeod. The effects of inhomogeneities and anisotropies on electrocardiographic fields: A 3-D finite element study. *IEEE Trans. Biomed. Eng.*, 44:706–719, 1997.

[71] C. Ramanathan and Y. Rudy. Electrocardiographic imaging: I. Effect of torso inhomogeneities on body surface electrocardiographic potentials. *J. Cardiovasc. Electrophysiol.*, 12:229–240, 2001.

[72] A. van Oosterom. The use of the spatial covariance in computing pericardial potentials. *IEEE Trans. Biomed. Eng.*, 46:778–787, 1999.

[73] C. Ramanathan and Y. Rudy. Electrocardiographic imaging: II. Effect of torso inhomogeneities on noninvasive reconstruction of epicardial potentials, electrograms, and isochrones. *J. Cardiovasc. Electrophysiol.*, 12:241–252, 2001.

[74] R. McFee and S. Rush. Qualitative effects of thoracic resistance variation on the interpretation of electrocardiograms: The low resistance surface layer. *Am. Heart J.*, pages 48–61, 1968.

[75] R.S. MacLeod and D.H. Brooks. Validation approaches for electrocardiographic inverse problems. In P. Johnston, editor, *Advances in Computational Biomedicine (Volume 3)*, pages 229–268.

[76] M.P. Nash and A.J. Pullan. Challenges facing validation of noninvasive electrical imaging of the heart. *Ann. Noninvasive Electrophysiol.*, 10:73–82, 2005.

[77] A.M. Katz. *Physiology of the Heart.* Raven Press, 2nd edition, 1992.

[78] D. Li, C.Y. Li, A.C. Yong, P.R. Johnston, and D. Kilpatrick. Epicardial ST depression in acute myocardial infarction. *Circ. Res.*, 85:959–964, 1999.

[79] B. Hopenfeld, J.G. Stinstra, and R.S. MacLeod. Mechanism for ST depression associated with contiguous subendocardial ischemia. *J. Cardiocasc. Electrophysiol.*, 15:1200–1206, 2004.

[80] B. Hopenfeld, J.G. Stinstra, and R.S. MacLeod. The effect of conductivity on ST-segment epicardial potentials arising from subendocardial ischemia. *Ann. Biomed. Eng.*, 33:751–763, 2005.

[81] M.C. MacLachlan, J. Sundnes, and G.T. Lines. Simulation of ST segment changes during subendocardial ischemia using a realistic 3-D cardiac geometry. *IEEE Trans. Biomed. Eng.*, 52:799–807, 2005.

[82] M. Potse, R. Coronel, S. Falcao, A-R. LeBlanc, and A. Vinet. The effect of lesion size and tissue remodeling on ST deviation in partial-thickness ischemia. *Heart Rhythm*, 4:200–206, 2007.

[83] D. Li, C.Y. Li, A.C. Yong, and D. Kilpatrick. Source of electrocardiographic ST changes in subendocardial ischemia. *Circ. Res.*, 82:925–970, 1998.

[84] K. Thygesen, J.S. Alpert, and H.D. White; on behalf of the Joint ESC/ACCF/AHA/WHF Task Force for the redefinition of myocardial infarction. Universal definition of myocardial infarction. *Circulation*, 116:2634–2653, 2007.

[85] E. Pueyo, L. Sörnmo, and P. Laguna. QRS slopes for detection and characterization of myocardial ischemia. *IEEE Trans. Biomed. Eng.*, 55:468–477, 2008.

[86] J. Pettersson, O. Pahlm, E. Carro, L. Edenbrandt, M. Ringborn, L. Sörnmo, S.G. Warren, and G.S. Wagner. Changes in high-frequency QRS components are more sensitive than ST-deviation for detecting acute coronary artery occlusion. *J. Amer. Coll. Cardiol*, 36:1827–1834, 2000.

[87] B.M. Horáček and G.S. Wagner. Electrocardiographic ST-segment changes during acute myocardial ischemia. *Cardiac Electrophysiol. Rev.*, 6:196–203, 2002.

[88] F. Kornreich. Identification of best electrocardiographic leads for diagnosing acute myocardial ischemia. *J. Electrocardiol.*, 31 Suppl.:157–163, 1998.

[89] S-F. Wung and B. Drew. Comparison of 18-lead ECG and selected body surface potential mapping leads in determining maximally deviated ST lead and efficacy in detecting acute myocardial ischemia during coronary occlusion. *J. Electrocardiol.*, 32 Suppl.:30–36, 1999.

[90] R.S. MacLeod. *Percutaneous Transluminal Coronary Angioplasty as a Model of Cardiac Ischemia: Clinical and Modelling Studies.* PhD thesis, Dalhousie University, 1990.

[91] K. Simelius. *Development of cardiographic mapping techniques for clinical use.* Licentiate thesis, Helsinki University of Technology, 1998.

[92] A.M. Lincoff and E.J. Topol. Interventional catheterization techniques. In E. Braunwald, editor, *Heart disease: a textbook of cardiovascular medicine*, pages 1366–1391. W.B. Saunders, 5th edition, 1997.

[93] Texas Heart Institute. Coronary artery disease. http://www.texasheart.org/HIC/Anatomy/coroanat.cfm, May 2008.

[94] H. Väänänen, P. Korhonen, J. Montonen, M. Mäkijärvi, J. Nenonen, L. Oikarinen, K. Simelius, L. Toivonen, and T. Katila. Non-invasive arrhythmia risk evaluation in clinical environment. *Herzschrittmachertherapie und Elektrophysiologie*, 11:229–234, 2000.

[95] T.F. Oostendorp, A. van Oosterom, and G. Huiskamp. Interpolation on a triangulated 3D surface. *J. Comput. Phys.*, 80:331–343, 1989.

[96] P. Grande, B.F. Hansen, C. Christiansen, and J. Naestoft. Acute myocardial infarct size estimated by serum CK–MB determinations: Clinical accuracy and prognostic relevance utilizing a practical modification of the isoenzyme approach. *Amer. Heart J.*, 101:582–586, 1981.

[97] J. Carpenter and J. Bithell. Bootstrap confidence intervals: when, which, what? A practical guide for medical statisticians. *Stat. Med.*, 19:1141–1164, 2000.

[98] B. Efron and R.J. Tibshirani. *An Introduction to the Bootstrap.* Chapman and Hall, 1993.